An efficient numerical model for the simulation of coupled heat, air and moisture transfer in porous media

Julien Berger, Denys Dutykh, Nathan Mendes, Laurent Gosse

An efficient numerical model for the simulation of coupled heat, air and moisture transfer in porous media

Julien Berger [a*], Denys Dutykh[b], Nathan Mendes[c] and Laurent Gosse[d]

December 16, 2019

[a] Univ. Grenoble Alpes, Univ. Savoie Mont Blanc, CNRS, LOCIE, 73000 Chambéry, France
[b] Univ. Grenoble Alpes, Univ. Savoie Mont Blanc, CNRS, LAMA, 73000 Chambéry, France
[c] Thermal Systems Laboratory, Mechanical Engineering Graduate Program, Pontifical Catholic University of Paraná, Rua Imaculada Conceição, 1155, CEP: 80215-901, Curitiba – Paraná, Brazil
[d] Istituto per le Applicazioni del Calcolo "Mauro Picone" (CNR), Via dei Taurini, 19, 00185 Rome, Italy
*corresponding author, e-mail address : julien.berger@univ-smb.fr

Abstract

This article proposes an efficient explicit numerical model with a relaxed stability condition for the simulation of heat, air and moisture transfer in porous material. Three innovative approaches are combined to solve the system of two differential advection–diffusion equations coupled with a purely diffusive equation. First, the Du Fort–Frankel scheme is used to solve the diffusion equation, providing an explicit scheme with an extended stability region. Then, the two advection–diffusion equations are solved using both the Scharfetter–Gummel numerical scheme for the space discretisation and the two–step Runge–Kutta method for the time variable. This combination enables to relax the stability condition by one order. The proposed numerical model is evaluated on three case studies. The first one considers quasi-linear coefficients. The theoretical results of the numerical schemes are confirmed by our computations. Indeed, the stability condition is relaxed by a factor of 40 compared to the standard Euler explicit approach. The second case provides an analytical solution for a weakly nonlinear problem. A very satisfactory accuracy is observed between the reference solution and the one provided by the numerical model. The last case study assumes a more realistic application with nonlinear coefficients and Robin-type boundary conditions. The computational time is reduced 10 times by using the proposed model in comparison with the explicit Euler method.

Key words: transfer in porous media; numerical model; Scharfetter–Gummel scheme; Du Fort–Frankel scheme; two-step Runge–Kutta method

Contents

1 Introduction **2**

2 Formulation of the mathematical model **4**

3 The numerical model **7**
3.1 Numerical strategy 7
3.2 Spatial discretisation 9
3.2.1 The moisture mass balance equation (3a), ... 9
3.2.2 The energy balance equation (3b) 10
3.2.3 The moist air mass balance equation (3c) 11
3.2.4 Treating the boundary conditions 12
3.3 Temporal discretisation 13
3.3.1 The moisture mass and energy balance equations (3a) and (3b) . . 13
3.3.2 The moist air mass balance equation (3c) 14
3.4 Extension to nonlinear coefficients 15
3.5 Important features of the numerical scheme 16
3.6 Metrics for evaluating the efficiency a numerical model 17

4 Validation of the numerical model **17**
4.1 First case study: the importance of relaxing the stability condition 19
4.2 Second case: comparison with analytical solutions 23
4.3 Third case: Robin boundary conditions and a fully nonlinear problem . . . 32

5 Conclusion **34**

6 Nomenclature **38**

1 Introduction

The prediction of heat and moisture transfer in porous material is of great interest for several applications such as food [1], civil construction [2] or soil evaporation [3]. Generally, the air transfer are neglected to simplify the mathematical model and particularly its numerical resolution as realized in [4, 5]. However, the air transfer might impact significantly the heat and mass processes by the presence of advective flux. Several recent works demonstrated that the air transfer should not be neglected to ensure the reliability of the model prediction. In [6], the impact of air transfer was highlighted using an experimental approach. In [7, 8], a numerical model, based on a commercial software, was used to investigate the impact of air transfer on the heat and mass transfer in a porous material. Recently, in [9], the numerical predictions have been compared to experimental observation to evaluate the reliability of the model. It was clearly shown that the fidelity of the model is improved when considering the three governing equations.

The mathematical model for the prediction of heat, air and moisture transfer in porous material is formulated as a system of two advection–diffusion differential equations completed with one exclusively diffusion equation (see [9, 10] for the derivation):

$$c_m \cdot \frac{\partial P_1}{\partial t} \;=\; \boldsymbol{\nabla} \cdot \left(k_m \cdot \boldsymbol{\nabla} P_1 \;-\; \boldsymbol{a}_v \cdot P_1 \right), \tag{1a}$$

$$\begin{aligned} c_q \cdot \frac{\partial T}{\partial t} \;=\; & \boldsymbol{\nabla} \cdot \left(k_q \cdot \boldsymbol{\nabla} T \;-\; \boldsymbol{a}_q \cdot T \right) \;+\; r_{12} \cdot \boldsymbol{\nabla} \cdot \left(k_v \cdot \boldsymbol{\nabla} P_1 \;-\; \boldsymbol{a}_v \cdot P_1 \right) \\ & -\; r_{12} \cdot c_{qv} \cdot \frac{\partial P_1}{\partial t} \;+\; r_{12} \cdot c_{qs} \cdot \frac{\partial \sigma}{\partial t}, \end{aligned} \tag{1b}$$

$$\begin{aligned} c_a \cdot \frac{\partial P}{\partial t} \;=\; & \boldsymbol{\nabla} \cdot \left(k_a \cdot \boldsymbol{\nabla} P \right) \;-\; \boldsymbol{\nabla} \cdot \left(k_v \cdot \boldsymbol{\nabla} P_1 \;-\; \boldsymbol{a}_v \cdot P_1 \right) \\ & +\; c_{av} \cdot \frac{\partial P_1}{\partial t} \;+\; c_{at} \cdot \frac{\partial T}{\partial t} \;+\; c_{as} \cdot \frac{\partial \sigma}{\partial t}, \end{aligned} \tag{1c}$$

where $T(\boldsymbol{x}, t)$, $P_1(\boldsymbol{x}, t)$, $P(\boldsymbol{x}, t)$ are the temperature, vapor pressure, air pressure and saturation rate in the porous material[1]. This model is used in several practical case studies for the investigation of the physical phenomena as, for instance, in [8, 11]. Thus, it is of capital importance to propose an efficient numerical model. The main issue in the numerical resolution is twofold. First, from a physical point of view, the following asymptotic inequality can be stated for the permeability coefficients:

$$k_a \;\gg\; \max \left\{ k_v, k_m, k_q \right\}.$$

Therefore, in the framework of explicit approaches, a very restrictive stability Courant-Friedrichs-Lewy (CFL) condition is imposed by the air transfer equation [12]. It necessarily implies very fine time discretisation at the price of important computational efforts. The second issue arises from the nonlinearities of the coefficients k, c and a that induce sharp gradients and lead to oscillations of the solution. Thus, when using implicit approaches, costly subiterations associated with Jacobian evaluation to treat the nonlinearities are required at each time step. Even if the stability restriction is overcome, these subiterations increase the computational time of these approaches. In addition, to satisfy the accuracy, the time step used generally scales with the one required within explicit approaches [13, Section 2.1][2]. Some authors also report that numerical schemes such as Crank–Nicolson combined with a central finite-difference scheme in space lead to spurious oscillations for advection–diffusion equation [14].

Several models from the literature are based on these approaches being constrained by these issues. In [6, 8, 11], an implicit numerical model is proposed. To overcome the restrictions, authors simplify the boundary conditions [6] or use linear coefficients [8]. It is still an

[1] Other symbols are described in the nomenclature section.

[2] The order of accuracy is $\varepsilon \;=\; \mathcal{O}\left(\Delta t^{\,\lambda} \;+\; \Delta x^{\,\mu} \right)$. Usually, $\lambda \;=\; 1$ for the implicit Euler and $\mu \;=\; 2$ for central finite–differences. Thus, to reach a satisfactory accuracy, it is required to balance error terms $\dfrac{\Delta t}{\Delta x^{\,2}} \simeq 1$. It implies that $\Delta t \;=\; \mathcal{O}\left(\Delta x^{\,2} \right)$.

open challenge to propose efficient numerical models that reduce computational costs and maximize the accuracy of the solution. To address this issue, the present article presents an explicit numerical model with much less restrictive stability conditions than the standard CFL one. The proposed model is based on a combination of three innovative approaches: *(i)* the Du Fort–Frankel scheme, *(ii)* the Scharfetter–Gummel approaches and *(iii)* the two–step Runge–Kutta method. It results in a study at the frontier between the domains of applied mathematics and heat and mass transfer in porous materials. To our knowledge, these methods have very few practical applications and have never been combined to solve the coupled governing equations of heat, air and mass transfer in porous material.

The paper is organized as follows. In Section 2, the mathematical model is defined in a dimensionless formulation. Then, the methods to build the efficient numerical model are detailed in Section 3. The spatial and time discretization of the governing equations are presented. In Section 4, the efficiency of the proposed numerical model is evaluated on three case studies. The first one is quasi-linear and enables to verify the theoretical results of the numerical schemes in terms of reducing the stability condition. The second one proposes to evaluate the accuracy of the numerical model with a derived exact analytical solution. The last case deals with more realistic ones considering nonlinear coefficients.

2 Formulation of the mathematical model

The achievement of the mathematical mode (1) to describe the physical phenomena of heat, air and moisture transfer occurring in porous media is highlighted in [9]. A one-dimensional problem is considered. While performing a mathematical and numerical analysis of a given practical problem, it is of capital importance to obtain a unitless formulation of governing equations [15, 16]. Thus, the following dimensionless quantities for temperature, vapor pressure and total pressure fields are defined:

$$u : \Big(x\,,\, t \Big) \longmapsto \frac{P_1\,(x\,,\,t\,)}{T^{\circ}}\,, \quad v : \Big(x\,,\, t \Big) \longmapsto \frac{T\,(x\,,\,t\,)}{P_1^{\circ}}\,, \quad w : \Big(x\,,\, t \Big) \longmapsto \frac{P\,(x\,,\,t\,)}{P^{\circ}}\,,$$

where the super-script $^{\circ}$ denotes the reference value of the field, chosen according to the physical situation. The saturation rate σ in the material is given by a function of the dimensionless fields:

$$\sigma : \Big(u\,,\, v\,,\, w \Big) \longmapsto \sigma \Big(u\,,\, v\,,\, w \Big)\,.$$

The time and space domains are also transformed through a dimensionless representation:

$$x^{\star} : \Big[0\,,\, L \Big] \longrightarrow \Big[0\,,\, 1 \Big] \qquad\qquad t^{\star} : \Big[0\,,\, \tau \Big] \longrightarrow \Big[0\,,\, \tau^{\star} \Big]$$
$$x \longmapsto \frac{x}{L}\,, \qquad\qquad t \longmapsto \frac{t}{t^{\circ}}\,,$$

where $L\ \left[\,\mathsf{m}\,\right]$ is the characteristic length of the material, $\tau\ \left[\,\mathsf{s}\,\right]$ is the final time of the simulation and t° a reference time value.

$$c^{\star}_{ic}\ :\ \Big(\,u\,,\,v\,,\,w\,\Big) \longmapsto \frac{c_{ic}\Big(\,u\,,\,v\,,\,w\,\Big)}{c^{\circ}_{ic}}\,,$$

$$k^{\star}_{ik}\ :\ \Big(\,u\,,\,v\,,\,w\,\Big) \longmapsto \frac{k_{ik}\Big(\,u\,,\,v\,,\,w\,\Big)}{k^{\circ}_{ik}}\,,$$

$$a^{\star}_{ia}\ :\ \Big(\,u\,,\,v\,,\,w\,\Big) \longmapsto \frac{a_{ia}\Big(\,u\,,\,v\,,\,w\,\Big)}{a^{\circ}_{ia}}\,,$$

where $ic \in \Big\{\,m\,,\,a\,,\,q\,,\,qv\,,\,qs\,,\,av\,,\,at\,,\,as\,\Big\}$, $ik \in \Big\{\,m\,,\,q\,,\,a\,,\,v\,\Big\}$ and $a \in \Big\{\,v\,,\,q\,\Big\}$. In this way, dimensionless numbers are introduced. The Péclet number represents the relative importance of the advection over the diffusion transfer processes for moisture, vapor and heat quantities:

$$\mathrm{Pe}_m \overset{\text{def}}{:=} \frac{a^{\circ}_v \cdot L}{k^{\circ}_m}\,, \qquad \mathrm{Pe}_v \overset{\text{def}}{:=} \frac{a^{\circ}_v \cdot L}{k^{\circ}_v}\,, \qquad \mathrm{Pe}_q \overset{\text{def}}{:=} \frac{a^{\circ}_q \cdot L}{k^{\circ}_q}\,.$$

The Fourier number reflects the importance of the total transfer for moisture, heat or air diffusion:

$$\mathrm{Fo}_m \overset{\text{def}}{:=} \frac{k^{\circ}_m \cdot t^{\circ}}{c^{\circ}_m \cdot L^{\,2}}\,, \qquad \mathrm{Fo}_q \overset{\text{def}}{:=} \frac{k^{\circ}_q \cdot t^{\circ}}{c^{\circ}_q \cdot L^{\,2}}\,, \qquad \mathrm{Fo}_a \overset{\text{def}}{:=} \frac{k^{\circ}_a \cdot t^{\circ}}{c^{\circ}_a \cdot L^{\,2}}\,.$$

The vaporization latent heat is transformed into a dimensionless ratio $r^{\star} \overset{\text{def}}{:=} \dfrac{r_{12}}{r^{\circ}_{12}}$. Other parameters are also introduced to characterize the importance of coupling among the phenomena:

$$\gamma \overset{\text{def}}{:=} \frac{r^{\circ}_{12} \cdot P^{\circ}_1 \cdot k^{\circ}_1}{T^{\circ} \cdot k^{\circ}_q}\,, \qquad \delta \overset{\text{def}}{:=} \frac{P^{\circ}_1 \cdot k^{\circ}_1}{P^{\circ} \cdot k^{\circ}_a}\,,$$

The Kossovitch number quantities of heat of the evaporation process to the wetting body:

$$\mathrm{Ko}_{qv} \overset{\text{def}}{:=} \frac{r^{\circ}_{12} \cdot c^{\circ}_{qv} \cdot P^{\circ}_1}{c^{\circ}_q \cdot T^{\circ}}\,.$$

Likewise, analogous numbers are introduced :

$$\mathrm{Ko}_{qs} \overset{\text{def}}{:=} \frac{r^{\circ}_{12} \cdot c^{\circ}_{qs}}{c^{\circ}_q \cdot T^{\circ}}\,, \quad \mathrm{Ko}_{av} \overset{\text{def}}{:=} \frac{c^{\circ}_{av} \cdot P^{\circ}_1}{c^{\circ}_a \cdot P^{\circ}}\,, \quad \mathrm{Ko}_{as} \overset{\text{def}}{:=} \frac{c^{\circ}_{as}}{c^{\circ}_a \cdot P^{\circ}}\,, \quad \mathrm{Ko}_{at} \overset{\text{def}}{:=} \frac{c^{\circ}_{at} \cdot T^{\circ}}{c^{\circ}_a \cdot P^{\circ}}\,.$$

For the boundary conditions, the BIOT number quantifies the transfer by diffusion (of moisture or heat) to the transfer between the material and the ambient air:

$$\mathrm{Bi}_m \overset{\text{def}}{:=} \frac{\alpha_m \cdot L}{k_m}, \qquad \mathrm{Bi}_q \overset{\text{def}}{:=} \frac{\alpha_q \cdot L}{k_q}, \qquad \mathrm{Bi}_v \overset{\text{def}}{:=} \frac{r_{12}^{\circ} \cdot \alpha_m \cdot L}{k_v},$$

where $\alpha_q \left[\mathsf{W/m^2 \cdot K}\right]$ and $\alpha_m \left[\mathsf{s/m}\right]$ are the surface heat and vapor transfer coefficients, respectively.

Consequently, the dimensionless one-dimensional formulation of the heat, air and moisture transfer in porous material can be written as:

$$c_m^\star \cdot \frac{\partial u}{\partial t^\star} = \mathrm{Fo}_m \cdot \frac{\partial}{\partial x^\star}\left(k_m^\star \cdot \frac{\partial u}{\partial x^\star} - \mathrm{Pe}^m \cdot a_v^\star \cdot u \right), \tag{2a}$$

$$\begin{aligned} c_q^\star \cdot \frac{\partial v}{\partial t^\star} &= \mathrm{Fo}_q \cdot \frac{\partial}{\partial x^\star}\left(k_q^\star \cdot \frac{\partial v}{\partial x^\star} - \mathrm{Pe}^q \cdot a_q^\star \cdot v \right) \\ &\quad + \mathrm{Fo}_q \cdot \gamma \cdot r^\star \cdot \frac{\partial}{\partial x^\star}\left(k_v^\star \cdot \frac{\partial u}{\partial x^\star} - \mathrm{Pe}^v \cdot a_v^\star \cdot u \right) \\ &\quad - \mathrm{Ko}_{qv} \cdot c_{qv}^\star \cdot r^\star \cdot \frac{\partial u}{\partial t^\star} + \mathrm{Ko}_{qs} \cdot c_{qs}^\star \cdot r^\star \cdot \frac{\partial \sigma}{\partial t^\star}, \end{aligned} \tag{2b}$$

$$\begin{aligned} c_a^\star \cdot \frac{\partial w}{\partial t^\star} &= \mathrm{Fo}_a \cdot \frac{\partial}{\partial x^\star}\left(k_a^\star \cdot \frac{\partial w}{\partial x^\star} \right) - \mathrm{Fo}_a \cdot \delta \cdot \frac{\partial}{\partial x^\star}\left(k_v^\star \cdot \frac{\partial u}{\partial x^\star} - \mathrm{Pe}^v \cdot a_v^\star \cdot u \right) \\ &\quad + \mathrm{Ko}_{av} \cdot c_{av}^\star \cdot \frac{\partial u}{\partial t^\star} + \mathrm{Ko}_{as} \cdot c_{as}^\star \cdot \frac{\partial \sigma}{\partial t^\star} + \mathrm{Ko}_{at} \cdot c_{at}^\star \cdot \frac{\partial v}{\partial t^\star}, \end{aligned} \tag{2c}$$

with the following boundary conditions at the air-material interface:

$$\begin{aligned} k_m^\star \cdot \frac{\partial u}{\partial x^\star} - \mathrm{Pe}^m \cdot a_m^\star \, u &= \mathrm{Bi}_m \cdot \left(u - u_\infty \right) \cdot \eta, \\ k_q^\star \cdot \frac{\partial v}{\partial x^\star} - \mathrm{Pe}^q \cdot a_q^\star \cdot v + \gamma \cdot r^\star \cdot \left(k_v^\star \cdot \frac{\partial u}{\partial x^\star} - \mathrm{Pe}^v \cdot a_v^\star \cdot u \right) &= \\ \mathrm{Bi}_q \cdot \left(v - v_\infty \right) \cdot \eta + \gamma \cdot \mathrm{Bi}_v \cdot r^\star \cdot \left(u - u_\infty \right) \cdot \eta, \\ w &= w_\infty . \end{aligned}$$

At the end, the mathematical model is represented by a system of three coupled nonlinear partial differential equations. The first two equations are based on the advection and diffusion phenomena while the third equation is purely based on diffusion with coupling done through source terms. The moisture equation (2a) influences Eqs. (2b) and (2c) directly through source terms in their respective right-hand sides. The air transfer equation (2c), impacts the other balances through the advection coefficient $a^\star$, which is proportional to the spatial derivative w. It should be noticed that the dimensionless numbers are constants. Parameters $c^\star$, $k^\star$ and $a^\star$ depend on the fields u, v and w enforcing the coupling

between the equations of system (2). These coefficients translate the nonlinearity of the problem and represent the deviation from the reference state.

3 The numerical model

3.1 Numerical strategy

After presenting the mathematical model, the numerical method to solve the governing equation is presented. For the sake of notation compactness, the super-script * is omitted in this section. Before, the numerical strategy is commented with the issue of reducing the computational effort and maximizing the accuracy of the solution. First, due to the nonlinearities of the problem, an explicit scheme is preferred since implicit approaches require costly subiterations to treat them at each time step. Secondly, as mentioned in the Introduction, the air transfer can be faster that for heat and moisture. So the following inequalities can be set for the FOURIER numbers:

$$\mathrm{Fo}_a \gg \max\left\{ \mathrm{Fo}_v \,,\, \mathrm{Fo}_m \,,\, \mathrm{Fo}_q \right\}.$$

Therefore, in the framework of explicit EULER approaches, the stability condition is imposed by the air transfer equation (2c) [12]:

$$\Delta t \leqslant \frac{\Delta x^2}{\mathrm{Fo}_a} \cdot \inf_{\mathrm{Dom}\, c_a \cap \mathrm{Dom}\, k_a} \left\{ \frac{c_a\left(u\,,\,v\,,\,w\right)}{k_a\left(u\,,\,v\,,\,w\right)} \right\}.$$

To circumvent the highlighted difficulties, the numerical strategy proposes first to solve equation (2c) by using the DU FORT–FRANKEL scheme to relax extensively its stability condition. Then, for the heat and mass advection–diffusion equations (2a) and (2b), the SCHARFETTER–GUMMEL numerical scheme is used. Preliminary studies [17, 18] showed the efficiency of the approach to extend the stability conditions and the accuracy of the solution. As a last step of the proposed methodology, the time discretisation of these two equations, an innovative two-step RUNGE–KUTTA approach is used of the time discretisation of these two advection–diffusion equations, enabling to extend further the stability region of the numerical scheme [19]. Since the method of lines is used to solve the problem, first the spatial discretisation is presented for each equation of the system (2). Then, the time integration to solve the système of coupled ordinary differential equations is detailed.

A uniform discretisation is considered for space and time intervals. The discretisation step parameters are denoted using Δx for space and Δt for time. The spatial cell $\mathcal{C}_j \overset{\text{def}}{:=} \left[x_{j\,-\,\frac{1}{2}} \,,\, x_{j\,+\,\frac{1}{2}} \right]$ is shown in Figure 1(a). The discrete values of the function u are denoted by $u_j^n \overset{\text{def}}{:=} u(\,x_j\,,\,t^n\,)$ with $j \in \left\{ 1\,,\ldots,N \right\}$ and $n \in \left\{ 1\,,\ldots,N_t \right\}$.

To explain the numerical method, the system of Eqs. (2) will be written using a simpler notation, removing the super-script $\star$, gathering the dimensionless numbers and consider-

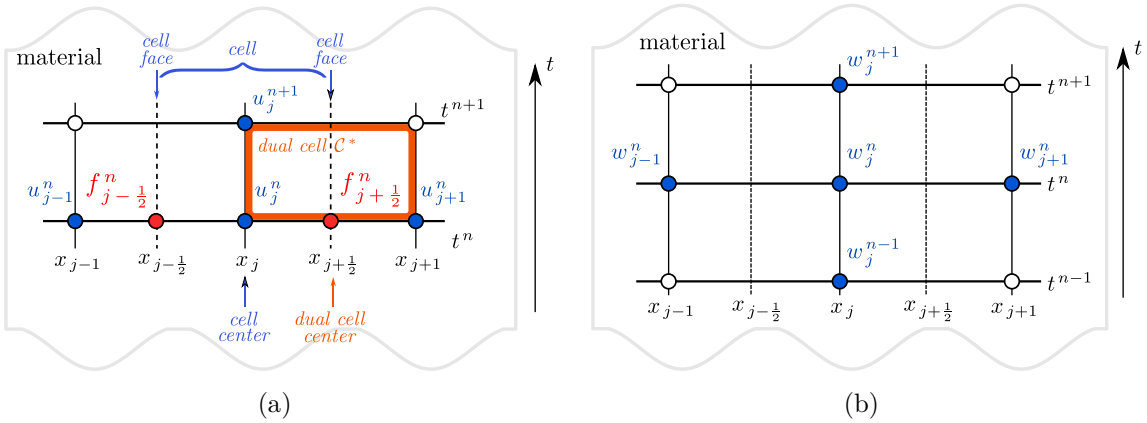

(a) (b)

Figure 1. *Stencils of the* Scharfetter–Gummel *(a) and* Du Fort–Frankel *(b) schemes.*

ing a linear problem for $x \in \left[0\,,\,1\right]$ and $t > 0$:

$$\frac{\partial u}{\partial t} = \frac{\partial f}{\partial x}\,, \tag{3a}$$

$$\frac{\partial v}{\partial t} = \frac{\partial g}{\partial x} + S\,, \tag{3b}$$

$$\frac{\partial w}{\partial t} = \frac{\partial h}{\partial x} + \Sigma\,, \tag{3c}$$

where

$$f \stackrel{\text{def}}{:=} k_1 \cdot \frac{\partial u}{\partial x} - a_1 \cdot u\,,$$

$$g \stackrel{\text{def}}{:=} k_{22} \cdot \frac{\partial v}{\partial x} - a_{22} \cdot v + k_{21} \cdot \frac{\partial u}{\partial x} - a_{21} \cdot u\,, \quad S \stackrel{\text{def}}{:=} -c_{21} \cdot \frac{\partial u}{\partial t} + c_{2s} \cdot \frac{\partial \sigma}{\partial t}\,,$$

$$h \stackrel{\text{def}}{:=} k_{33} \cdot \frac{\partial w}{\partial x} - k_{31} \cdot \frac{\partial u}{\partial x} + a_{31} \cdot u\,, \qquad \Sigma \stackrel{\text{def}}{:=} c_{31} \cdot \frac{\partial u}{\partial t} + c_{32} \cdot \frac{\partial v}{\partial t} + c_{3s} \cdot \frac{\partial \sigma}{\partial t}\,.$$

The extension to the nonlinear problem is detailed in Section 3.4. One can note that, in the system of Eqs. (3), the partial coefficients c_1, c_2 and c_3 has been omitted for the sake of clarity in front of the partial derivatives $\frac{\partial u}{\partial t}$, $\frac{\partial v}{\partial t}$ and $\frac{\partial w}{\partial t}$, respectively. Their integration do not present any specific difficulties since the system is triangular. So at each time step, the inversion of the storage coefficients is straightforward using analytical approach.

3.2 Spatial discretisation

3.2.1 The moisture mass balance equation (3a),

The discretisation of Eq. (3a) gives the following semi-discrete difference differential relation:

$$\frac{\mathrm{d}u_j}{\mathrm{d}t} \;=\; \frac{1}{\Delta x}\cdot\left[\, f_{j+\frac{1}{2}} \;-\; f_{j-\frac{1}{2}} \,\right].$$

Initially proposed in [20], the Scharfetter–Gummel scheme assumes that the numerical flux is constant on the dual cell $\mathcal{C}_j^\star \stackrel{\text{def}}{:=} \left[\, x_j \,,\, x_{j+1} \,\right]$, which is illustrated in Figure 1(a). According to the definition of f, the following boundary value problem can be written [21, 22] to determine the numerical flux:

$$k_1\cdot\frac{\partial u}{\partial x} \;-\; a_1\cdot u \;=\; f_{j+\frac{1}{2}}\,, \qquad \forall\, x \,\in\, \mathcal{C}_j^\star\,, \qquad \forall\, j \,\in\, \Big\{\, 2\,,\,\ldots\,,\,N \;-\; 1 \,\Big\}\,, \tag{4a}$$

$$u \;=\; u_j\,, \qquad x \;=\; x_j\,, \tag{4b}$$

$$u \;=\; u_{j+1}\,, \qquad x \;=\; x_{j+1}\,. \tag{4c}$$

It is important to remark that the the boundary value problem (4) has two unknowns $f_{j+\frac{1}{2}}$ and $u \,:\, \mathcal{C}^\star \stackrel{\text{def}}{:=} \bigcup\limits_{j\,\in\,[\![1,N]\!]} \mathcal{C}_j^\star \;\longrightarrow\; \mathbb{R}$ with two boundary conditions. Therefore, the exact expression of the flux in the dual cell can be computed as [23]:

$$f_{j+\frac{1}{2}} \;=\; \frac{d_1}{\Delta x}\cdot\left[\, \mathcal{B}\Big(\,\Theta\,\Big)\cdot u_{j+1} \;-\; \mathcal{B}\Big(\,-\,\Theta\,\Big)\cdot u_j \,\right], \tag{5}$$

where $\mathcal{B}$ stands for the reciprocal Bernoulli function $\mathcal{B} \,:\, \mathbb{R} \;\longrightarrow\; \mathrm{R}_{>0}$

$$\mathcal{B}\,(\,y\,) \;\stackrel{\text{def}}{:=}\; \frac{y}{\mathrm{e}^{\,y} \;-\; 1}\,, \qquad\qquad \Theta \;\stackrel{\text{def}}{:=}\; \frac{a_1\cdot\Delta x}{k_1}\,.$$

Furthermore, the exact solution u can be computed from the boundary value problem (4):

$$u\,(\,x\,) \;=\; -\,\frac{1}{a_1}\cdot f_{j+\frac{1}{2}} \;+\; K_j\cdot \mathrm{e}^{\;\frac{a_1\,\cdot\,x}{k_1}}\,, \qquad\qquad \forall\, x \,\in\, \mathcal{C}_j^\star\,, \tag{6}$$

where

$$K_j \;\stackrel{\text{def}}{:=}\; \frac{\Big(\,u_j \;-\; u_{j+1}\,\Big)}{1 \;-\; \mathrm{e}^{\,\Theta}}\cdot \mathrm{e}^{\;-\,\frac{a_1\,\cdot\,x_j}{k_1}}$$

is a defined constant, which depends on the boundary value problem data.

Two important consequences can be obtained from these two results. First, the semi-discrete difference differential relation for Eq. (3a) becomes:

$$\frac{\mathrm{d}u_j}{\mathrm{d}t} \;=\; \frac{d_1}{\Delta x}\cdot\left[\mathcal{B}\big(\Theta\big)\cdot u_{j+1} \;-\; \Big(\mathcal{B}\big(\Theta\big) \;+\; \mathcal{B}\big(-\Theta\big)\Big)\cdot u_j \;+\; \mathcal{B}\big(-\Theta\big)\cdot u_{j-1}\right]. \quad (7)$$

Then, the exact solution avoids any need of interpolation to compute the field in the whole domain of the material, *i.e.* in between the nodes.

3.2.2 The energy balance equation (3b)

The Scharfetter–Gummel numerical scheme is also used for the the spatial discretisation of Eq. (3b). The semi-discrete difference relation yields:

$$\frac{\mathrm{d}v_j}{\mathrm{d}t} \;=\; \frac{1}{\Delta x}\cdot\left[g_{j+\frac{1}{2}} \;-\; g_{j-\frac{1}{2}}\right] \;+\; S_j\,. \quad (8)$$

Similarly, the numerical flux $g_{j+\frac{1}{2}}$ is assumed to be constant on the dual cell $\mathcal{C}_j^\star$. So, the following boundary value problem can be written:

$$k_{22}\cdot\frac{\partial v}{\partial x} \;-\; a_{22}\cdot v \;=\; g_{j+\frac{1}{2}} \;-\; \underbrace{k_{21}\cdot\frac{\partial u}{\partial x} \;+\; a_{21}\cdot u}_{\text{known}}, \quad \forall\, x\in\mathcal{C}_j^\star, \quad \forall\, j\in\Big\{2,\ldots,N\;-\;1\Big\}, \quad (9a)$$

$$v \;=\; v_j\,, \qquad x \;=\; x_j\,, \quad (9b)$$

$$v \;=\; v_{j+1}\,, \qquad x \;=\; x_{j+1}\,. \quad (9c)$$

By Eq. (6), the exact solution $u\,(\,x\,)$ is already known for $x\in\mathcal{C}_j^\star$. Thus, Eq. (9a) can be replaced to reformulate the boundary value problem:

$$k_{22}\cdot\frac{\partial v}{\partial x} \;-\; a_{22}\cdot v \;=\; g_{j+\frac{1}{2}} \;-\; k_{21}\cdot\frac{a_1}{k_1}\cdot K_j\cdot \mathrm{e}^{\frac{a_1\cdot x}{k_1}} \quad (10a)$$

$$+\; a_{21}\cdot\left(-\frac{1}{a_1}\cdot f_{j+\frac{1}{2}} \;+\; K_j\cdot\mathrm{e}^{\frac{a_1\cdot x}{k_1}}\right), \quad \forall\, x\in\mathcal{C}_j^\star, \quad \forall\, j\in\Big\{2,\ldots,N\;-\;1\Big\},$$

$$v \;=\; v_j\,, \qquad x \;=\; x_j\,, \quad (10b)$$

$$v \;=\; v_{j+1}\,, \qquad x \;=\; x_{j+1}\,. \quad (10c)$$

Two unknowns of Eq. (10), v and $g_{j+\frac{1}{2}}$, can be computed. The computation is accomplished in the supplementary `Maple`™ file. This approach considers a full coupling between Eqs. (3a) and (3b).

The coupling source term $S_j \overset{\text{def}}{:=} -c_{21} \cdot \dfrac{\mathrm{d}u_j}{\mathrm{d}t} + c_{2s} \cdot \dfrac{\mathrm{d}\sigma_j}{\mathrm{d}t}$ is evaluated using Eq. (7) for the first right-hand side term $-c_{21} \cdot \dfrac{\mathrm{d}u_j}{\mathrm{d}t}$. For the second right-hand side term $c_{2s} \cdot \dfrac{\mathrm{d}\sigma_j}{\mathrm{d}t}$, a backward finite–difference approach in the time domain is used:

$$\left.\frac{\mathrm{d}\sigma_j}{\mathrm{d}t}\right|_{t\,=\,t^n} = \frac{1}{\Delta t} \cdot \left(\sigma\left(u_j^n, v_j^n\right) - \sigma\left(u_j^{n-1}, v_j^{n-1}\right) \right). \tag{11}$$

3.2.3 The moist air mass balance equation (3c)

For Eq. (3c), we have the following semi-discrete difference differential elation:

$$\frac{\mathrm{d}w_j}{\mathrm{d}t} = \frac{1}{\Delta x} \cdot \left[h_{j+\frac{1}{2}} - h_{j-\frac{1}{2}} \right] + \Sigma_j \,,$$

where the numerical flux $h_{j+\frac{1}{2}}$ is given by:

$$h_{j+\frac{1}{2}} = \left(k_{33} \cdot \frac{\partial w}{\partial x} - k_{31} \cdot \frac{\partial u}{\partial x} + a_{31} \cdot u \right)\Bigg|_{j+\frac{1}{2}}. \tag{12}$$

From Eq. (6), we have the exact solution of $u\,(\,x\,)$ that enables to compute the second and third terms of the right-hand side of Eq. (12):

$$\begin{aligned} -\,k_{31} \cdot \left.\frac{\partial u}{\partial x}\right|_{j+\frac{1}{2}} + a_{31} \cdot u_{j+\frac{1}{2}} \overset{(6)}{=} & -k_{31} \cdot \frac{a_1}{k_1} \cdot K_j \cdot \mathrm{e}^{\dfrac{a_1 \cdot x_{j+\frac{1}{2}}}{k_1}} \\ & + a_{31} \cdot \left(-\frac{1}{a_1} \cdot f_{j+\frac{1}{2}} + K_j \cdot \mathrm{e}^{\dfrac{a_1 \cdot x_{j+\frac{1}{2}}}{k_1}} \right), \end{aligned}$$

The first term of the right-hand side of Eq. (12) is driven by diffusion only, so it is approximated using central finite–difference scheme:

$$k_{33} \cdot \left.\frac{\partial w}{\partial x}\right|_{j+\frac{1}{2}} = k_{33} \cdot \frac{w_{j+1} - w_j}{\Delta x}\,.$$

Then, the numerical flux $h_{j+\frac{1}{2}}$ is computed as:

$$h_{j+\frac{1}{2}} = k_{33} \cdot \frac{w_{j+1} - w_j}{\Delta x} - k_{31} \cdot \frac{a_1}{k_1} \cdot K_j \cdot \mathrm{e}^{\dfrac{a_1 \cdot x_{j+\frac{1}{2}}}{k_1}} + a_{31} \cdot \left(-\frac{1}{a_1} \cdot f_{j+\frac{1}{2}} + K_j \cdot \mathrm{e}^{\dfrac{a_1 \cdot x_{j+\frac{1}{2}}}{k_1}} \right).$$

Finally, the semi-discrete difference differential relation for Eq. (3c) becomes:

$$\frac{\mathrm{d}w_j}{\mathrm{d}t} = \frac{k_{33}}{\Delta x^2}\cdot\left(w_{j+1} - 2\cdot w_j + w_{j-1}\right) \tag{13}$$

$$- \frac{k_{31}\cdot a_1}{\Delta x\cdot k_1}\cdot\left(K_j\cdot \mathrm{e}^{\frac{a_1\cdot x_{j+\frac{1}{2}}}{k_1}} - K_{j-1}\cdot \mathrm{e}^{\frac{a_1\cdot x_{j-\frac{1}{2}}}{k_1}}\right) \tag{14}$$

$$- \frac{a_{31}}{a_1}\cdot\left(f_{j+\frac{1}{2}} - f_{j-\frac{1}{2}}\right) + a_{31}\cdot\left(K_j\cdot \mathrm{e}^{\frac{a_1\cdot x_{j+\frac{1}{2}}}{k_1}} - K_{j-1}\cdot \mathrm{e}^{\frac{a_1\cdot x_{j-\frac{1}{2}}}{k_1}}\right) + \Sigma_j\,. \tag{15}$$

The source term $\Sigma_j \overset{\text{def}}{:=} c_{31}\cdot\frac{\mathrm{d}u_j}{\mathrm{d}t} + c_{32}\cdot\frac{\mathrm{d}v_j}{\mathrm{d}t} + c_{3s}\cdot\frac{\mathrm{d}\sigma_j}{\mathrm{d}t}$ is evaluated using Eqs. (7), (8) and (11) for each term.

3.2.4 Treating the boundary conditions

To explain the implementation of the Scharfetter–Gummel approach for the nodes adjacent to the boundary surface, we assume a Robin–type condition for the field u:

$$k_1\cdot\frac{\partial u}{\partial x} - a_1\cdot u = \mathrm{Bi}\cdot\left(u - u_\infty\right), \qquad x = 0\,.$$

Thus, Eq. (4) defines the boundary value problem to compute the leftmost numerical flux $f_{\frac{1}{2}}$, which is written as:

$$k_1\cdot\frac{\partial u}{\partial x} - a_1\cdot u = f_{\frac{1}{2}}\,, \qquad \forall\, x\in\left[0\,,\,x_1\right], \tag{16a}$$

$$k_1\cdot\frac{\partial u}{\partial x} - a_1\cdot u = \mathrm{Bi}\cdot\left(u - u_\infty\right), \qquad x = 0\,, \tag{16b}$$

$$u = u_1^n\,, \qquad x = x_1\,. \tag{16c}$$

By solving problem (16), we get:

$$f_{\frac{1}{2}} : \Theta \longrightarrow a_1\cdot\mathrm{Bi}\cdot\frac{u_1^n - u_\infty\cdot\mathrm{e}^{\Theta}}{a_1\cdot\mathrm{e}^{\Theta} + \mathrm{Bi}\cdot\left(\mathrm{e}^{\Theta} - 1\right)}\,.$$

Similar approach can be applied to the boundary conditions at $x = 1$ and for the field v. Furthermore, It can be extended to any type (Neumann or Dirichlet) of boundary condition along the directions given above. Interested readers are invited to consult [18] for more details.

3.3 Temporal discretisation

As previously mentioned, the stability restriction is essentially imposed by Eq. (3c). It will be relaxed by using the Du Fort–Frankel scheme presented in Section 3.3.2. It provides a highly stable explicit scheme. Thus, it is expected that the stability restriction will be imposed by the two other Equations (3a) and (3b). So, to relax their stability conditions, it is proposed to use an explicit two–step Runge–Kutta methods [24]. Thus, this strategy for the temporal discretisation provides a competitive option compared to classical methods such as explicit Euler, one-step Runge–Kutta or implicit.

3.3.1 The moisture mass and energy balance equations (3a) and (3b)

For the description of the temporal discretisation, Eqs. (3a) and (3b) are written as an initial value problem:

$$\begin{aligned} \frac{\partial u}{\partial t} &= F(u), & F(u) &= \frac{\partial f}{\partial x}, \\ \frac{\partial v}{\partial t} &= G(v), & G(v) &= \frac{\partial g}{\partial x} + S. \end{aligned}$$

The following fully discrete scheme is obtained using the Two-Step Runge–Kutta (TSRK) methods [19]:

$$u^{n+1} = \theta \cdot u^{n-1} + \Big(1 - \theta\Big) \cdot u^{n} + \Delta t \cdot \sum_{k=1}^{s} \Big[\nu_k \cdot F\Big(U_k^{n-1} \Big) + \mu_k \cdot F\Big(U_k^{n} \Big) \Big],$$

$$U_k^{n} = \lambda_k \cdot u^{n-1} + \Big(1 - \lambda_k\Big) \cdot u^{n} + \Delta t \cdot \sum_{p=1}^{s} \Big[a_{kp} \cdot F\Big(U_p^{n-1} \Big) + b_{kp} \cdot F\Big(U_p^{n} \Big) \Big]$$

and for v:

$$v^{n+1} = \theta \cdot v^{n-1} + \Big(1 - \theta\Big) \cdot v^{n} + \Delta t \cdot \sum_{k=1}^{s} \Big[\nu_k \cdot G\Big(V_k^{n-1} \Big) + \mu_k \cdot G\Big(V_k^{n} \Big) \Big],$$

$$V_k^{n} = \lambda_k \cdot v^{n-1} + \Big(1 - \lambda_k\Big) \cdot v^{n} + \Delta t \cdot \sum_{p=1}^{s} \Big[a_{kp} \cdot G\Big(V_p^{n-1} \Big) + b_{kp} \cdot G\Big(V_p^{n} \Big) \Big],$$

where θ, ν_k, μ_k, λ_k, a_{kp} and b_{kp} are numerical coefficients given in [19]. They depend on the number of stages s. Here, the numerical model is built for $s \in \Big\{ 1, 2, 3 \Big\}$, whose

coefficients are provided in the following BUTCHER tableaux [19]:

$$\begin{array}{c||c|c} \lambda_k & a_{kp} & b_{kp} \\ \hline\hline \Theta & \nu_k & \mu_k \end{array}\,, \qquad \begin{array}{c||c|c} 0.1 & 0.2 & 0 \\ \hline\hline -1 & -1 & 1 \end{array}\,,$$

$$s \qquad\qquad s \;=\; 1$$

$$\begin{array}{c||cc|c} 0.308343 & 0.154172 & 0.154172 & \\ -0.113988 & -0.556994 & 0.00838564 & 1.43462 \\ \hline\hline 0 & -0.526458 & 0.0787465 & 1.47417 \quad -0.0264581 \end{array}\,,$$

$$s \;=\; 2$$

$$\begin{array}{c||ccc|ccc} 0.0213802 & 0.264446 & -0.507512 & 0.264446 & 0 & 0 & 0 \\ 0.0991119 & 0.240292 & -0.631471 & 0.597963 & 0.392328 & 0 & 0 \\ 0.353437 & 0.0969341 & -0.578148 & 0.98944 & 0.582927 & 0.262283 & 0 \\ \hline\hline 0 & 0.197972 & -0.543131 & 0.521515 & 0.0867149 & 0.621047 & 0.115883 \end{array}\,.$$

$$s \;=\; 3$$

3.3.2 The moist air mass balance equation (3c)

Using the form of Eq. (13), the semi-discrete spatial discretisation of Eq. (3c) with the method of (vertical) lines [25], is given by:

$$\frac{\mathrm{d}w_j}{\mathrm{d}t} \;=\; \frac{k_{33}}{\Delta x^2} \cdot \Big(w_{j+1} \;-\; 2 \cdot w_j \;+\; w_{j-1} \Big) \;+\; H_j \,, \tag{18}$$

where

$$H_j \;=\; \frac{k_{31} \cdot a_1}{\Delta x \cdot k_1} \cdot \left(K_j \cdot \mathrm{e}^{\dfrac{a_1 \cdot x_{j+\frac{1}{2}}}{k_1}} \;-\; K_{j-1} \cdot \mathrm{e}^{\dfrac{a_1 \cdot x_{j-\frac{1}{2}}}{k_1}} \right)$$
$$-\; \frac{a_{31}}{a_1} \cdot \Big(f_{j+\frac{1}{2}} \;-\; f_{j-\frac{1}{2}} \Big) \;+\; a_{31} \cdot \left(K_j \cdot \mathrm{e}^{\dfrac{a_1 \cdot x_{j+\frac{1}{2}}}{k_1}} \;-\; K_{j-1} \cdot \mathrm{e}^{\dfrac{a_1 \cdot x_{j-\frac{1}{2}}}{k_1}} \right) \;+\; \Sigma_j \,.$$

Using the so-called DU FORT–FRANKEL scheme [26], the term $2\,w_j^n$ is replaced by $w_j^{n+1} + w_j^{n-1}$. The stencil is illustrated in Figure 1(b). Thus, Eq. (18) becomes:

$$\frac{w_j^{n+1} \;-\; w_j^{n-1}}{2 \cdot \Delta t} \;=\; \frac{k_{33}}{\Delta x^2} \cdot \Big(w_{j+1}^n \;-\; \big(w_j^{n-1} \;+\; w_j^{n+1} \big) \;+\; w_{j-1}^n \Big) \;+\; H_j^n \,,$$

Re-arranging the last equation to express w_j^{n+1}, one obtains:

$$w_j^{n+1} \;=\; \frac{1 \;-\; \delta}{1 \;+\; \delta} \cdot w_j^{n-1} \;+\; \frac{\delta}{1 \;+\; \delta} \cdot \Big(u_{j+1}^{n} \;+\; w_{j-1}^{n} \Big) \;+\; \frac{2 \cdot \Delta t}{1 \;+\; \delta} \cdot H_j^{n} \,,$$

where

$$\delta \;\stackrel{\text{def}}{:=}\; \frac{2 \cdot \Delta t}{\Delta x^{\,2}} \cdot k_{33} \,.$$

According to the standard VON NEUMANN stability analysis, the DU FORT–FRANKEL scheme is unconditionally stable [27, 28]. Further details and examples of applications of this scheme may be consulted in [27, 29].

3.4 Extension to nonlinear coefficients

As mentioned before, the coefficients c, k and a are functions of u, v and/or w. To extend the detailed numerical method to the nonlinear problem, one may consider the method of frozen coefficients on dual cell $\mathcal{C}_j^{\star}$. Thus, the boundary value problem Eq. (4) is written as:

$$f_{j+\frac{1}{2}} \;=\; k_{1\,,j+\frac{1}{2}} \cdot \frac{\partial u}{\partial x} \;-\; a_{1\,,j+\frac{1}{2}} \cdot u \,,$$

where the coefficients are computed as:

$$k_{1\,,j+\frac{1}{2}} \;=\; k_1 \Big(u_{j+\frac{1}{2}} \,,\, v_{j+\frac{1}{2}} \,,\, w_{j+\frac{1}{2}} \Big) \,, \qquad a_{1\,,j+\frac{1}{2}} \;=\; a_1 \Big(u_{j+\frac{1}{2}} \,,\, v_{j+\frac{1}{2}} \,,\, \frac{\partial w}{\partial x}\bigg|_{j+\frac{1}{2}} \Big) \,,$$

with

$$u_{j+\frac{1}{2}} \;=\; \frac{1}{2} \cdot \Big(u_{j+1} \;+\; u_j \Big) \,, \quad v_{j+\frac{1}{2}} \;=\; \frac{1}{2} \cdot \Big(v_{j+1} \;+\; v_j \Big) \,, \quad w_{j+\frac{1}{2}} \;=\; \frac{1}{2} \cdot \Big(w_{j+1} \;+\; w_j \Big) \,.$$

The space derivative $\left.\dfrac{\partial w}{\partial x}\right|_{j+\frac{1}{2}}$ is evaluated using a second-order approximation:

$$\left.\frac{\partial w}{\partial x}\right|_{j+\frac{1}{2}} \;=\; \frac{1}{\Delta x} \cdot \Big(w_{j+1} \;-\; w_j \Big) \,.$$

The numerical flux $f_{j\pm\frac{1}{2}}$ is then computed using the same methodology as described in Section 3.2.1. By analogy, the approach is extended for the computation of the fluxes $g_{j\pm\frac{1}{2}}$ and $h_{j\pm\frac{1}{2}}$.

3.5 Important features of the numerical scheme

We recall the important features of the numerical schemes. First, the Scharfetter–Gummel scheme is well balanced and asymptotically preserving [22]. Indeed, the following limiting behavior of Eq. (5) is observed:

$$\lim_{a_1 \to 0} f_{j+\frac{1}{2}} = d_1 \cdot \frac{u_{j+1} - u_j}{\Delta x}, \qquad \lim_{d_1 \to 0} f_{j+\frac{1}{2}} = \begin{cases} -a_1 \cdot u_j, & a_1 \leqslant 0, \\ -a_1 \cdot u_{j+1}, & a_1 > 0. \end{cases}$$

When the advection coefficient is much greater than the diffusion one, the expression of the numerical flux tends to the so-called upwind scheme. Inversely, when the diffusion coefficient is more important, the flux is approximated by central finite differences. Therefore, the flux is correct independently from the grid parameters. This property applies also to the numerical flux $g_{j+\frac{1}{2}}$ from Eq. (3b).

Secondly, the numerical model is built using an explicit expression for each governing equation of the system of Eqs. (3). Thus, no sub-iterations are needed at each time step to treat the nonlinearities of the problem. It enables to save important computational efforts.

An important advantage concerns the stability condition of the numerical scheme. Using the Du Fort–Frankel approach, the theoretical results ensure a highly stable explicit scheme to solve Eq. (3c). The choice for the discretisation parameters of this equation is also driven by the characteristic times of the physical phenomena. The numerical stability condition of the system of Eqs. (3) is therefore given by the scheme used for Eqs. (3a) and (3b). The Scharfetter–Gummel scheme combined with the Euler explicit in time approach has the following stability restriction [23]:

$$\Delta t \max_{1 \leqslant k,l \leqslant 2} \left(\max_{1 \leqslant j \leqslant N} k_{kl,j} \max_{1 \leqslant j \leqslant N} \left[\frac{a_{kl,j}}{k_{kl,j}} \tanh \left(\frac{a_{kl,j} \Delta x}{2 k_{kl,j}} \right)^{-1} \right] \right) \leqslant \Delta x. \tag{19}$$

As one may notice, the stability conditions of the latter equation is nonlinear with respect to Δx. For large space discretisation Δx, $\tanh \left(\frac{a_{kl,j} \Delta x}{2 k_{kl,j}} \right) = \mathcal{O}(1)$ and we obtain $\Delta t \leqslant C \Delta x$ [18]. Thus, it is one order less restrictive than standard approach and the so-called Courant-Friedrichs-Lewy (CFL) conditions $\Delta t \leqslant C \Delta x^2$. Using, the Scharfetter–Gummel scheme, the spatial discretisation does not need to be extremely refined. Furthermore, since the exact solutions u and v are known, no interpolation is required to compute the fields within the whole spatial domain. This observation is not true for the field w, which requires interpolation. Finally, the use of the two-step Runge–Kutta scheme for the temporal discretisation of Eqs. (3a) and (3b) enables to extend a little more the stability region, depending on the choice of the number of stages. A less restrictive condition than Eq. (19) is expected.

3.6 Metrics for evaluating the efficiency a numerical model

Several metrics are defined to compare the efficiency and accuracy of numerical models. The first one is the error with respect to a reference solution $u^{\mathrm{ref}}(x,t)$. It is computed as a function of x:

$$\varepsilon_2(x) \overset{\text{def}}{:=} \sqrt{\frac{1}{N_t}\sum_{n=1}^{N_t}\left(u(x,t^n) - u^{\mathrm{ref}}(x,t^n)\right)^2},$$

with N_t the number of temporal steps. The global error is given by:

$$\varepsilon_\infty \overset{\text{def}}{:=} \sup_{x \in \left[0,L\right]} \varepsilon_2(x),$$

The second criterion is the number of significative correct digits of the approximate solution, computed using results from [30]:

$$\mathrm{scd}(u) \overset{\text{def}}{:=} -\log_{10}\left\| \frac{u(x,\tau) - u^{\mathrm{ref}}(x,\tau)}{u^{\mathrm{ref}}(x,\tau)} \right\|_\infty.$$

The last criterion is the computational (CPU) time $t_{\mathrm{cpu}}\left[\mathtt{s}\right]$ spent by the numerical model to compute the solution. The measurement are carried out using the Matlab™ platform and a computer equipped with Intel i7 CPU and 32 GB of RAM. The ratio R_{cpu} is defined:

$$R_{\mathrm{cpu}} \overset{\text{def}}{:=} \frac{t_{\mathrm{cpu}}}{\tau},$$

where τ is the final physical time of the simulation, expressed in the same units as the CPU time t_{cpu} .

4 Validation of the numerical model

Three case studies are considered to evaluate the efficiency of the proposed numerical method. An illustration of the cases is shown in Figure 2. The first one represents an quasi-linear problem. Only the nonlinearity in the air velocity, operating the coupling between all three differential equations, is kept. This case highlights the relevance of relaxing the stability condition to solve the transient differential equation of air transfer. For the second case, an analytical solution is proposed as a reference solution to validate the numerical model. The problem considers a few nonlinearities in the transport coefficient. The last case study deals with a realistic configuration found in the building sector, *i.e.*, with nonlinear coefficients and Robin–type boundary conditions.

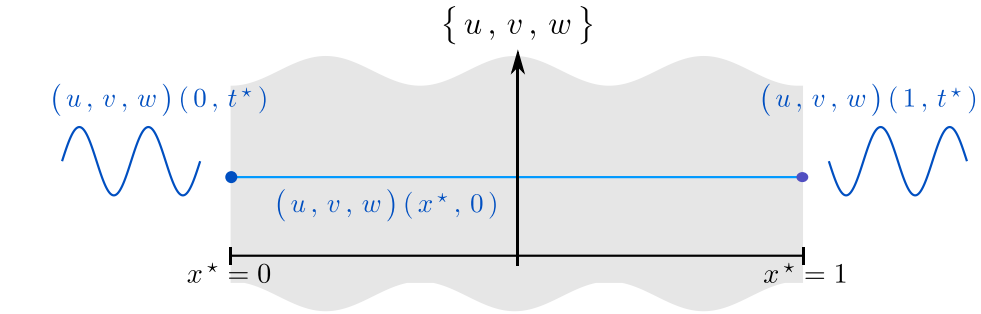

(a) Cases 1 & 3

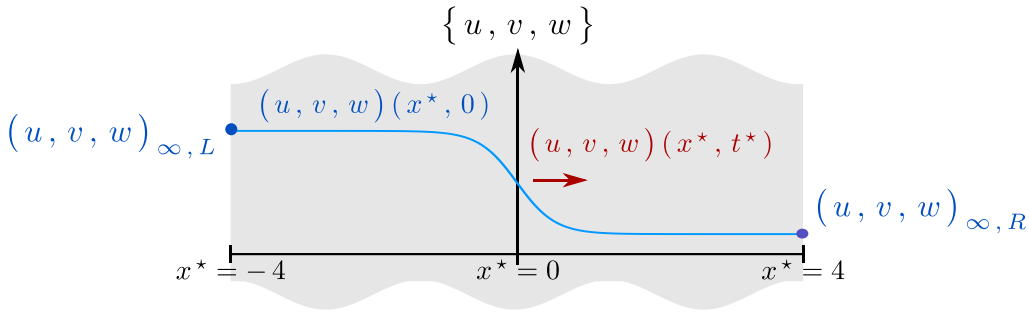

(b) Case 2

Figure 2. *Schematic description of three case studies for the validation of the numerical model.*

4.1 First case study: the importance of relaxing the stability condition

Here, the reference solution is computed using a numerical pseudo–spectral approach obtained with the `Matlab`™ open source toolbox `Chebfun` [31]. A dimensionless problem is considered with the following numerical values for the parameters:

$$\mathrm{Fo}_m = 4\cdot10^{-3},\quad \mathrm{Fo}_q = 4\cdot10^{-2},\quad \mathrm{Fo}_a = 4\cdot10^{-1},\quad \mathrm{Pe}_m = 2\cdot10^{-3},\quad \mathrm{Pe}_v = 3\cdot10^{-3},$$
$$\mathrm{Pe}_q = 5\cdot10^{-3},\quad \mathrm{Ko}_{qv} = 1\cdot10^{-2},\quad \mathrm{Ko}_{av} = 2\cdot10^{-2},\quad \gamma = 1.5\cdot10^{-3},\quad \delta = 3\cdot10^{-4}.$$

Other parameters are equal to zero, $\mathrm{Ko}_{as} = \mathrm{Ko}_{at} = \mathrm{Ko}_{qs} = \beta = 0$. Parameters $c^\star$, $k^\star$ and $r^\star$, representing the nonlinearities of the problem, are set to a constant (one in scaled variables). The purposes is to verify the theoretical results of the stability conditions of the equations, which are obtained for linear problems. The only nonlinearity of the problem is introduced through the advection coefficient:

$$a_m^\star = a_v^\star = a_q^\star = \frac{\partial w}{\partial x^\star}.$$

It translates the physical coupling between the three equations of System (3) through the air velocity expressed by Darcy's law approximation. For this case, Dirichlet-type unsteady boundary conditions are defined:

$$u(0,t^\star) = 0.6\left(\sin\left(\pi\,t^\star\right) + \sin\left(\frac{2\,\pi}{24}\,t^\star\right)\right),\qquad u(1,t^\star) = 0.9\,\sin\left(\frac{2\,\pi}{6}\,t^\star\right),$$
$$v(0,t^\star) = 1.2\left(\sin\left(\frac{2\,\pi}{5}\,t^\star\right) + \sin\left(\frac{2\,\pi}{24}\,t^\star\right)\right),\quad v(1,t^\star) = 0.5\,\sin\left(\frac{2\,\pi}{3}\,t^\star\right)^2,$$
$$w(0,t^\star) = 1.3\,\sin\left(\frac{2\,\pi}{6}\,t^\star\right),\qquad w(1,t^\star) = 0.7\left(\sin\left(\frac{2\,\pi}{4}\,t^\star\right) + \sin\left(\frac{2\,\pi}{24}\,t^\star\right)\right.$$

The initial condition is

$$u(x^\star,0) = v(x^\star,0) = w(x^\star,0) = \mathbf{0},$$

and the final simulation time $\tau^\star = 24$. An illustration of this case is shown in Figure 2(a). The efficiency of the numerical model proposed in Section 3 is evaluated according to the criteria defined in Section 3.6. The model is tested for different values of $s \in \left\{1,2,3\right\}$ for the two–step Runge–Kutta method as reported in Eq. (17).

The proposed numerical model will be compared to other approaches specified in Table 1. The Numerical Model 1 (NM1$_\star$) corresponds to the standard temporal discretisation using Euler explicit approach. The NM2 uses the Du Fort–Frankel scheme for the spatio-temporal discretisation of Eq. (2c) and a standard approach for others. The NM3$_s$ is the proposed one, for different values of parameter s.

The solutions u, v and w are computed using $\Delta x^\star = 0.01$ and $\Delta t^\star = 10^{-4}$ as discretisation parameters. As shown in Figure 3, there is a very good agreement between the solutions of all numerical models and the reference one. The time evolution of the fields is in perfect accordance with the boundary conditions. The time evolution of the dimensionless velocity $\dfrac{\partial w}{\partial x}$ is shown in Figure 4. A very satisfactory agreement is also observed. It can be noticed that the profiles are less sharp for w than for u and v, due particularly to a higher FOURIER number. For the sake of clarity, it should be noted that the solutions of $\mathrm{NM3}_1$ and $\mathrm{NM3}_2$ are not plotted in Figures 3 and 4. However, as shown in Figure 5, the error is less than 10^{-3} for u and v and at the order of 10^{-5} for w. It can be remarked that the errors are very similar among the numerical models since they have the same spatial discretisation. For this reason, the significant digits accuracy is similar for fields u and v for NM 1, 2, 3a, 3b and 3c. The only difference appears for the field w for $\mathrm{NM1}_\star$:

$$\mathrm{scd}\Big[\mathrm{NM1}\,;\,2\,,\,3a\,,\,3b\,,\,3c\,,u\Big] = 3.30\,, \qquad \mathrm{scd}\Big[\mathrm{NM1}\,;\,2\,,\,3a\,,\,3b\,,\,3c\,,v\Big] = 3.77\,,$$
$$\mathrm{scd}\Big[\mathrm{NM2}\,;\,3a\,,\,3b\,,\,3c\,,w\Big] = 5.04\,, \qquad \mathrm{scd}\Big[\mathrm{NM1}\,;w\Big] = 4.79\,.$$

It highlights that solutions u, v and w are computed with more than three or five digits of accuracy.

A parametric study has been carried out on the discretisation parameter $\Delta t^\star$. The global error ε_∞ is computed using the reference solution for an segment of variation $\Delta t^\star \in \Big[10^{-5}\,,\,10^{-1}\Big]$. The spatial discretisation is fixed to $\Delta x^\star = 0.01$. The error variation in Δt is illustrated in Figure 6 for five numerical models. First, according to the values of the numerical parameters, the stability condition can be evaluated for each equation of System (2):

$$\text{Eq. (2a)} \;:\; \Delta t^\star \leqslant 1.25\cdot 10^{-2}\,, \tag{20a}$$
$$\text{Eq. (2b)} \;:\; \Delta t^\star \leqslant 1.25\cdot 10^{-3}\,, \tag{20b}$$
$$\text{Eq. (2c)} \;:\; \Delta t^\star \leqslant 1.25\cdot 10^{-4}\,. \tag{20c}$$

These conditions are depicted in Figures 6(a), 6(c) and 6(e) with red vertical dashed lines. As for the real physical case study of transfer through a porous building material, the stability condition of the whole system of differential equations is fixed by the air transfer equation (2c). As a consequence, the $\mathrm{NM1}_\star$, based on the EULER explicit scheme, is not able to compute the solutions without respecting the stability condition given in Eq. (20c). These observations can be noticed in Figures 6(a), 6(c) and 6(e). Since the DU FORT–FRANKEL scheme is unconditionally stable, NM2 and $\mathrm{NM3}_3$ enable to compute a bounded solution w for values of Δt higher than the ones provided by the condition (20c) as illustrated in Figure 6(e). This restriction is relaxed by 10 thanks to the DU FORT–FRANKEL scheme. Consequently, using NM2, bounded solutions u and v can be computed until the stability conditions of Eqs. (2a) and (2b) are respected. As shown in Figures 6(a) and 6(c), NM2 diverges for $\Delta t^\star$ outside these conditions provided by Eqs. (20a) and (20b), respectively.

The benefits of using a two–step Runge–Kutta approach in NM3 is illustrated in Figures 6(b) and 6(d). It can be noted that solutions u and v are computed with a satisfactory accuracy beyond the stability conditions. The stability of NM3 increases with the parameter s. The ratio between the stability condition of Eqs. (2a) and (2b) and the last $\Delta t^\star$, providing a satisfactory accuracy for the NM3$_3$, scales with 4.

The relaxation of the stability condition with the proposed model is synthesized in Figure 6(f). The use of Du Fort–Frankel scheme enables to gain one order. Then, the combination of the Scharfetter–Gummel with the two–step Runge–Kutta can relax by 4 the restriction. All in all, the overall gain in the stability condition scales with 40 compared to standard approaches.

Figure 7(a) gives the variation of the error with the computational time required to obtain the solution. Even when increasing the time discretisation parameter Δt, the accuracy of the NM1$_\star$, based on explicit Euler scheme, remains stable and, unfortunately, the computational time increases significantly. For an error on the solution scaling with $\mathcal{O}(10^{-3})$, the NM3 enables to compute the solution 10 times faster than the NM1$_\star$. The computational time ratio between the three versions of the NM3 is constant and consistent with the theoretical results since NM3$_3$ requires approximately three times more operations. As mentioned before, the main advantages of NM3$_3$ is to relaxed the stability conditions accepting a little increase of the number of operations to solve.

To go further in the discussion, the solution is computed with three numerical models NM1$_\star$, NM2 and NM3$_3$ for different values of discretisation parameters $\Delta t^\star$ and $\Delta x^\star$. Figure 7(b) shows the limit on the plane $\left(\Delta x^\star, \Delta t^\star\right)$ enabling to compute a bounded solution. In this way, a sort of numerically observed stability condition for this almost linear problem is investigated. As noticed, the observed stability condition of NM1$_\star$ varies as a second order $\mathcal{O}(\Delta x^{\star\,2})$ of the discretisation parameter Δx in space. It is consistent since the stability condition is induced by one of the air transport equation and given by standard CFL condition. Then, it can be noted that for NM2, the stability condition is relaxed thanks to the Du Fort–Frankel scheme. A change can be observed on the slope at $\Delta x^\star = 2 \cdot 10^{-2}$ after which the stability condition is relaxed. As detailed in Section 3.5, this relaxation may be due to the Scharfetter–Gummel scheme which has a nonlinear stability condition scaling with $\sim \mathcal{O}(\Delta x^{\star\,2})$ for small space discretisation and with $\sim \mathcal{O}(\Delta x^\star)$ for large space discretisation. The stability condition of the NM3$_3$ is relaxed with a maximum ratio of 14 with NM2 and 166 with NM1$_\star$.

This analysis enhances the importance of using the Du Fort–Frankel scheme in our numerical model to avoid the restrictive stability conditions imposed by the air transfer equation (2c). Furthermore, the two–step Runge–Kutta approach is used for Eqs. (2a) and (2b) to relax by a factor of $\sim$ 50 the global stability condition of the problem.

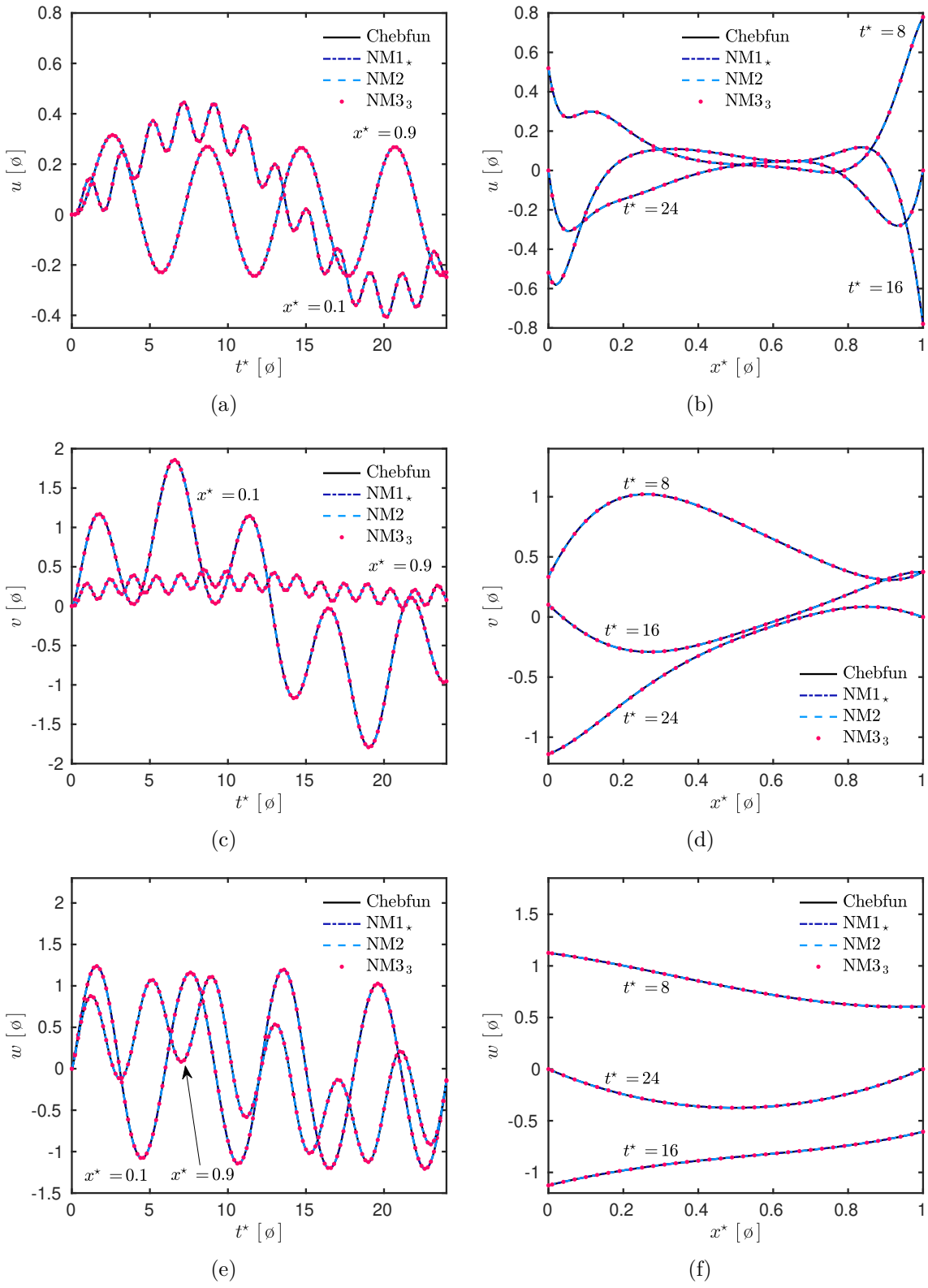

Figure 3. *Time evolution* (a, c, e) *and profiles* (b, d, d) *of the fields* u , v *and* w *for the first case study.*

Table 1. *Identification of the numerical models evaluated. Abbreviation* SG *stands for* Scharfetter–Gummel, DF *for* Du Fort–Frankel, TSRK *for two–step* Runge–Kutta, FD *for Finite–Difference,* Eu *for* Euler.

Numerical Model (NM)	Eqs. (2a) and (2c) discretisation		Eq. (2c) discretisation	
	Space	Time	Space	Time
NM1$_\star$	SG	Eu explicit	Central FD	Eu explicit
NM2	SG	Eu explicit	Central FD	DF
NM3$_1$	SG	TSRK, $s = 1$	Central FD	DF
NM3$_2$	SG	TSRK, $s = 2$	Central FD	DF
NM3$_3$	SG	TSRK, $s = 3$	Central FD	DF

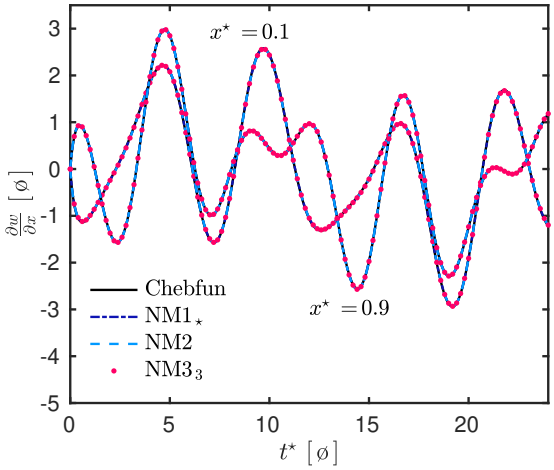

Figure 4. *Time evolution of the air velocity* $\dfrac{\partial w}{\partial x^\star}$ *at* $x^\star \in \left\{ 0.1\,,\, 0.9 \right\}$ *for the first case study.*

4.2 Second case: comparison with analytical solutions

In this Section, an analytical solution is proposed to validate the numerical scheme. To our knowledge, this solution seems to be presented for the very first time. An illustration of the case is provided in Figure 2(b). From a physical point of view, it represents the transfer of heat, air and moisture through a porous material with uniform initial conditions and submitted to a step of temperature, vapor pressure and air pressure at the boundaries. The evolution of the front of each field can be simulated. For this purpose, Eq. (2) is

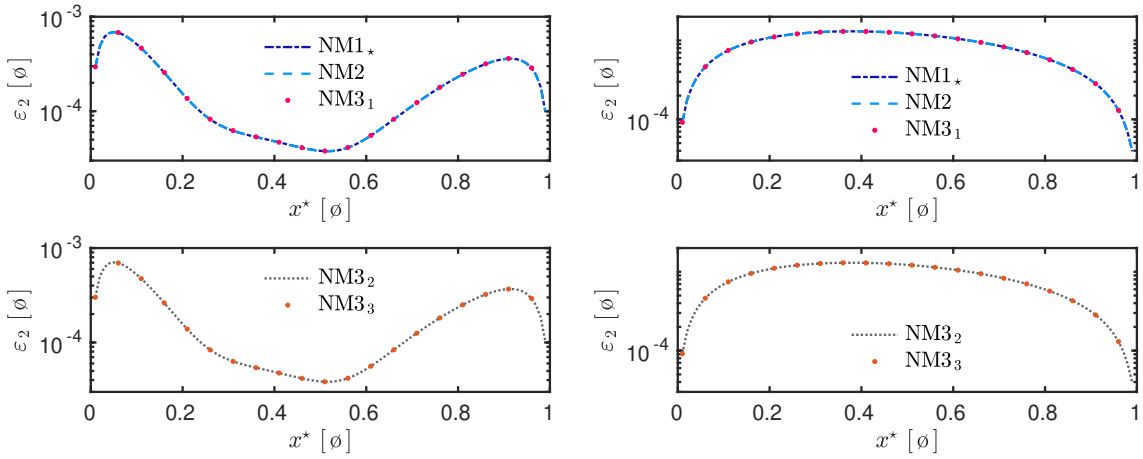

(a) for u

(b) for v

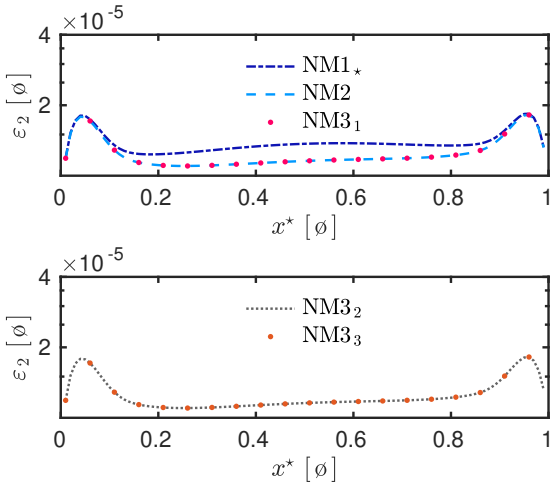

(c) for w

Figure 5. *Variation of the error ε_2 for the fields for the first case study.*

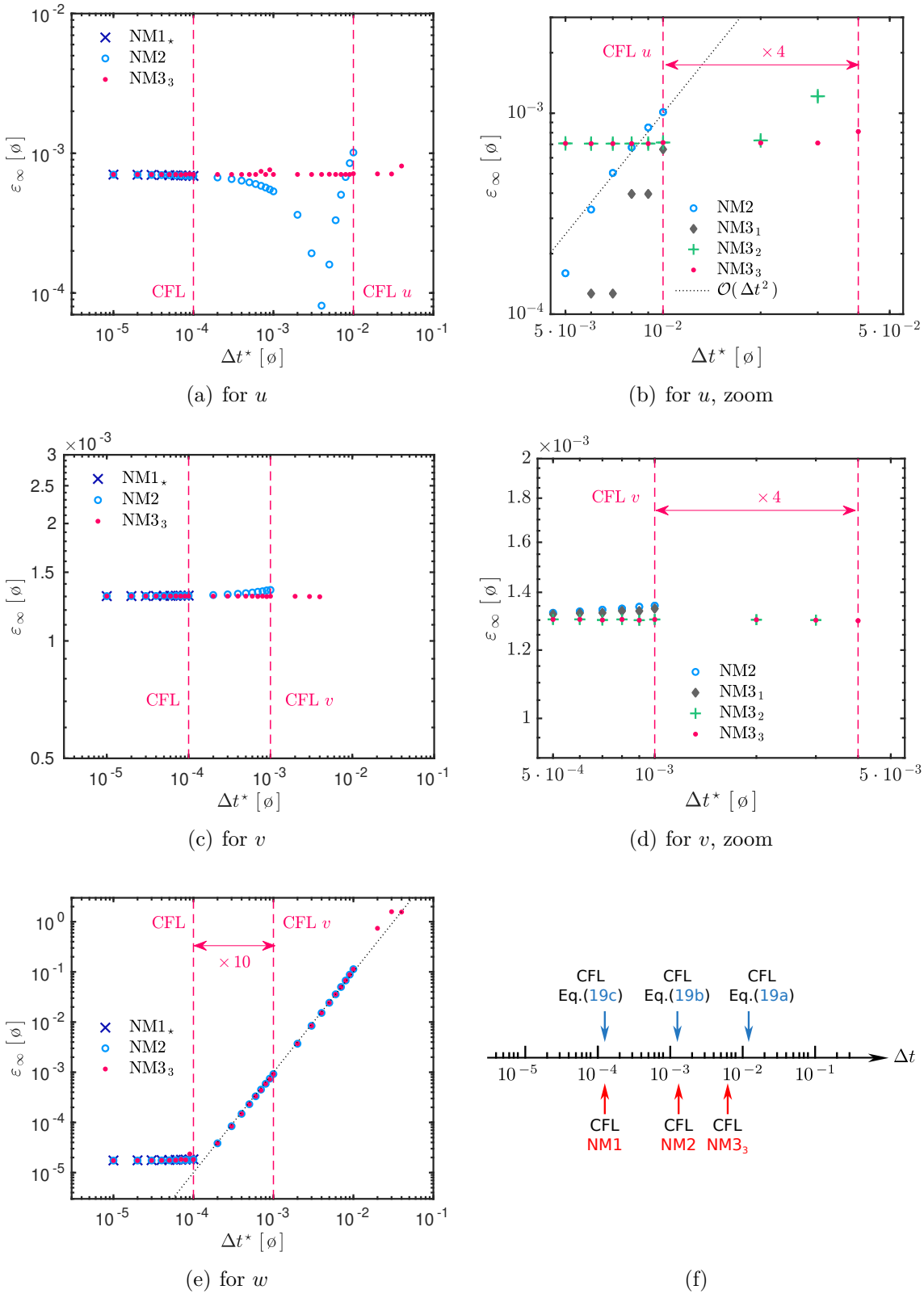

(a) for u (b) for u, zoom

(c) for v (d) for v, zoom

(e) for w (f)

Figure 6. *Variation of the error* ε_∞ (a, c, e) *for the fields* u, v *and* w *with an emphasis* (b, d) *around the stability condition for the first case study. Relaxation of the CFL condition* (e) *using* $NM3_3$.

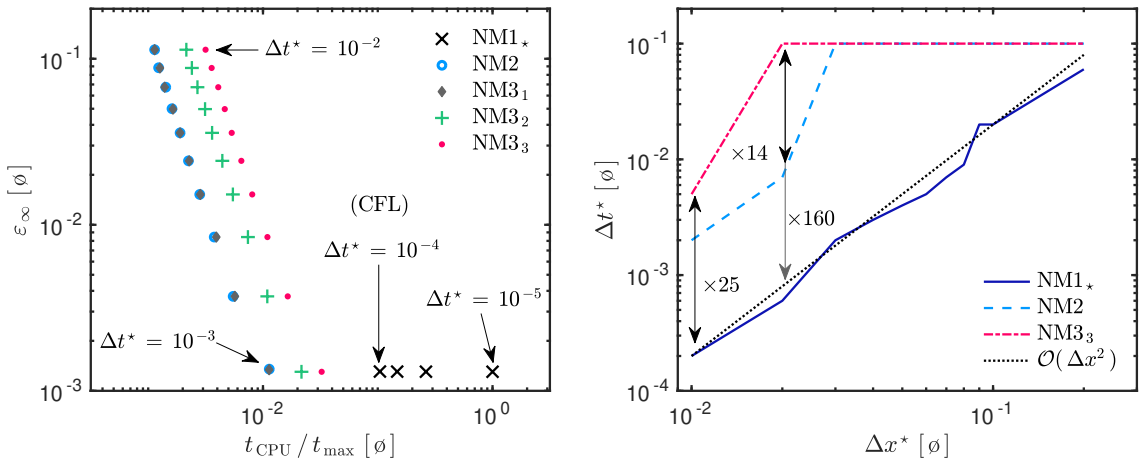

(a) (b)

Figure 7. *Variation of the error* ε_∞ (a) *of the numerical model with the computational time required to obtain the solution* ($t_{\max} = 316$ s). *Variation of the CFL stability condition* (b) *according to* $\Delta x^\star$ *and* $\Delta t^\star$ *for the numerical models for the first case study.*

written in the form:

$$c_1 \cdot \frac{\partial u}{\partial t^\star} = \frac{\partial}{\partial x^\star}\left(k_1 \cdot \frac{\partial u}{\partial x^\star} - a_1 \cdot u \right), \tag{21a}$$

$$c_2 \cdot \frac{\partial v}{\partial t^\star} = \frac{\partial}{\partial x^\star}\left(k_2 \cdot \frac{\partial v}{\partial x^\star} - a_2 \cdot v \right) + \frac{\partial}{\partial x^\star}\left(k_{21} \cdot \frac{\partial u}{\partial x^\star} - a_{21} \cdot u \right) - c_{21} \cdot \frac{\partial u}{\partial t^\star}, \tag{21b}$$

$$c_3 \cdot \frac{\partial w}{\partial t^\star} = \frac{\partial}{\partial x^\star}\left(k_3 \cdot \frac{\partial v}{\partial x^\star} \right) - \frac{\partial}{\partial x^\star}\left(k_{31} \cdot \frac{\partial u}{\partial x^\star} - a_{31} \cdot u \right) + c_{31} \cdot \frac{\partial u}{\partial t^\star}, \tag{21c}$$

with the particular case where:

$$a_1 = a_{10}\, u, \qquad a_2 = a_{20}\, v$$

and coefficients $\left(a_{10}, a_{20}, a_{21}, a_{31}, k_1, k_2, k_{21}, k_3, k_{31}, c_1, c_2, c_{21}, c_3, c_{31} \right)$ are constant. By direct substitution in Eq. (21), two analytical solutions can be obtained. Both solutions, $u(x^\star, t^\star)$ and $w(x^\star, t^\star)$ are invariant and written in the form:

$$u(x^\star, t^\star) = \frac{1}{2} \cdot j_u \cdot \tanh\left(k_u \cdot x^\star - c_u \cdot t^\star \right) + A_u,$$

$$w(x^\star, t^\star) = \frac{1}{2} \cdot j_w \cdot \tanh\left(k_w \cdot x^\star - c_w \cdot t^\star \right) + A_w,$$

with the coefficients defined by:

$$k_u \;=\; -\,\frac{a_{10}}{2\cdot k_1}\cdot j_u\,,\qquad c_u \;=\; \frac{1}{2\cdot k_1}\cdot\frac{a_{31}\cdot k_3\cdot a_{10}}{(\,k_{31}\cdot c_3\;-\;k_3\cdot c_{31}\,)}\cdot j_u\,,\qquad c_w \;=\; c_u\,,$$

$$k_w \;=\; k_u\,,\qquad\qquad A_u \;=\; -\,\frac{1}{2\cdot a_{10}}\cdot\frac{c_1\cdot k_3\cdot a_{31}}{(\,k_{31}\cdot c_3\;-\;k_3\cdot c_{31}\,)}\,,\qquad j_w \;=\; \frac{k_{31}}{k_3}\cdot j_u$$

and parameters j_u and A_w being free (defined by user). For the field $v(\,x^\star\,,\,t^\star\,)$, two solutions verify Eq. (21):

$$v_1(\,x^\star\,,\,t^\star\,) \;=\; \frac{1}{2}\cdot j_{v,1}\cdot\tanh\Big(\,k_{v,1}\cdot x^\star\;-\;c_{v,1}\cdot t^\star\,\Big)\;+\;A_{v,1}\,,$$

$$v_2(\,x^\star\,,\,t^\star\,) \;=\; \frac{1}{2}\cdot j_{v,2}\cdot\tanh\Big(\,k_{v,2}\cdot x^\star\;-\;c_{v,2}\cdot t^\star\,\Big)\;+\;A_{v,2}\,,$$

with coefficients:

$$k_{v,1} \;=\; k_{v,2} \;=\; k_u\,,$$

$$c_{v,1} \;=\; c_{v,2} \;=\; c_u\,,$$

$$j_{v,1} \;=\; \frac{-\,1}{2\cdot k_1\cdot a_{20}}\left(\,\sqrt{a_{10}^2\cdot k_2^2\;+\;4\cdot a_{10}\cdot a_{20}\cdot k_1\cdot k_{21}}\;-\;a_{10}\cdot k_2\,\right)\cdot j_u\,,$$

$$j_{v,2} \;=\; \frac{1}{2\cdot k_1\cdot a_{20}}\left(\,\sqrt{a_{10}^2\cdot k_2^2\;+\;4\cdot a_{10}\cdot a_{20}\cdot k_1\cdot k_{21}}\;+\;a_{10}\cdot k_2\,\right)\cdot j_u\,,$$

$$\begin{aligned}A_{v,1} \;=\; -\;\Bigg(&\frac{1}{2}\cdot\frac{a_{31}\cdot c_2\cdot k_3}{a_{20}}\cdot\Big(\,\sqrt{a_{10}^2\cdot k_2^2\;+\;4\cdot a_{10}\cdot a_{20}\cdot k_1\cdot k_{21}}\;-\;\;a_{10}\cdot k_2\,\Big)\\&-\;a_{21}\cdot c_3\cdot k_1\cdot k_{31}\;+\;a_{21}\cdot c_{31}\cdot k_1\cdot k_3\;-\;a_{31}\cdot c_{21}\cdot k_1\cdot k_3\Bigg)\\&\left(\Big(\,\sqrt{a_{10}^2\cdot k_2^2\;+\;4\cdot a_{10}\cdot a_{20}\cdot k_1\cdot k_{21}}\;-\;\;a_{10}\cdot k_2\,\Big)\,\Big(\,c_3\cdot k_{31}\;-\;c_{31}\cdot k_3\,\Big)\right)^{-1},\end{aligned}$$

$$\begin{aligned}A_{v,2} \;=\;&\left(\frac{-\,1}{2}\cdot\frac{a_{31}\cdot c_2\cdot k_3}{a_{20}}\cdot\Big(\,\sqrt{a_{10}^2\cdot k_2^2\;+\;4\cdot a_{10}\cdot a_{20}\cdot k_1\cdot k_{21}}\;+\;\;a_{10}\cdot k_2\,\Big)\right.\\&\left.-\;a_{21}\cdot c_3\cdot k_1\cdot k_{31}\;+\;a_{21}\cdot c_{31}\cdot k_1\cdot k_3\;-\;a_{31}\cdot c_{21}\cdot k_1\cdot k_3\right)\\&\left(\Big(\,\sqrt{a_{10}^2\cdot k_2^2\;+\;4\cdot a_{10}\cdot a_{20}\cdot k_1\cdot k_{21}}\;+\;\;a_{10}\cdot k_2\,\Big)\,\Big(\,c_3\cdot k_{31}\;-\;c_{31}\cdot k_3\,\Big)\right)^{-1}.\end{aligned}$$

The asymptotic values of $u(x^\star, t^\star = 0)$, $v(x^\star, t^\star = 0)$ and $w(x^\star, t^\star = 0)$ provide the DIRICHLET–type boundary conditions for the numerical models:

$$\lim_{x^\star \to \pm\infty} u(x^\star, 0) = u_{\infty,L/R}, \quad \lim_{x^\star \to \pm\infty} v(x^\star, 0) = v_{\infty,L/R}, \quad \lim_{x^\star \to \pm\infty} w(x^\star, 0) = w_{\infty,L/R}$$

An illustration of the case is shown in Figure 2(b). For the numerical application, the following values are used:

$$\begin{aligned} &c_1 = 1, \quad k_1 = 0.05, \quad a_{10} = 0.09, \quad c_2 = 1, \quad k_2 = 0.03, \quad a_{20} = 0.04, \quad c_{21} = 0.3, \\ &k_{21} = 0.01, \quad a_{21} = 0.03, \quad c_3 = 1, \quad k_3 = 0.6, \quad c_{31} = 0.6, \quad k_{31} = 0.18, \quad a_{31} = 0.2, \end{aligned}$$

with $j_u = 2.5$, $A_w = 0.5$ and, hence, the following boundary conditions:

$$\begin{aligned} u_{\infty,R} &= 2.45, & v_{\infty,R} &= 0.99, & w_{\infty,R} &= 0.13, \\ u_{\infty,L} &= 4.95, & v_{\infty,L} &= 0.30, & w_{\infty,L} &= 0.88. \end{aligned}$$

For the computations, the solutions of the numerical models are defined for the domains $\left(x^\star, t^\star\right) \in \left[-4, 4\right] \times \left[0, 3\right]$. This choice is justified since the solutions at the boundaries of the space domain $x \in \left\{-4, 4\right\}$ almost do not vary. Indeed, the $\mathcal{L}_2$ error between the imposed boundary conditions and the analytical solution is:

$$\begin{aligned} u_{\infty,R} : \varepsilon_2 &= 7.2 \cdot 10^{-5}, & u_{\infty,L} : \varepsilon_2 &= 8.9 \cdot 10^{-9}, \\ v_{\infty,R} : \varepsilon_2 &= 2.0 \cdot 10^{-5}, & v_{\infty,L} : \varepsilon_2 &= 2.5 \cdot 10^{-9}, \\ w_{\infty,R} : \varepsilon_2 &= 2.2 \cdot 10^{-5}, & w_{\infty,L} : \varepsilon_2 &= 2.7 \cdot 10^{-9}. \end{aligned}$$

The numerical solutions are computed using $\mathrm{NM3}_2$, $\mathrm{NM3}_3$, both defined in Table 1. The following discretisation parameters are used $\Delta x^\star = 10^{-2}$ and $\Delta t^\star = 10^{-4}$. A pseudo–spectral solution is also obtained with the `Matlab`™ open source toolbox `Chebfun` [31]. Comparison of the time evolution and profiles of the fields are shown in Figures 8 and 9. A perfect agreement can be noticed among three numerical solutions and the exact one. As noticed in Figure 10, the error is lower than 10^{-4} for each field. It can be noted that $\mathrm{NM3}_1$ and $\mathrm{NM3}_3$ have a very similar accuracy. This comparison highlights the high accuracy of the solution computed with the numerical models based on SCHARFETTER–GUMMEL and two–step RUNGE–KUTTA approaches.

It is important to notice that there is no uniqueness of the solution v for the problem (21) on the real line. Similar results were obtained by TYCHONOFF for the heat equation in [32]. Several criteria may be used to choose the reliable solution for v such as the entropy of the global system. In addition, when dealing with physical applications and adding boundary conditions to the problem, the uniqueness of the solution might be recovered.

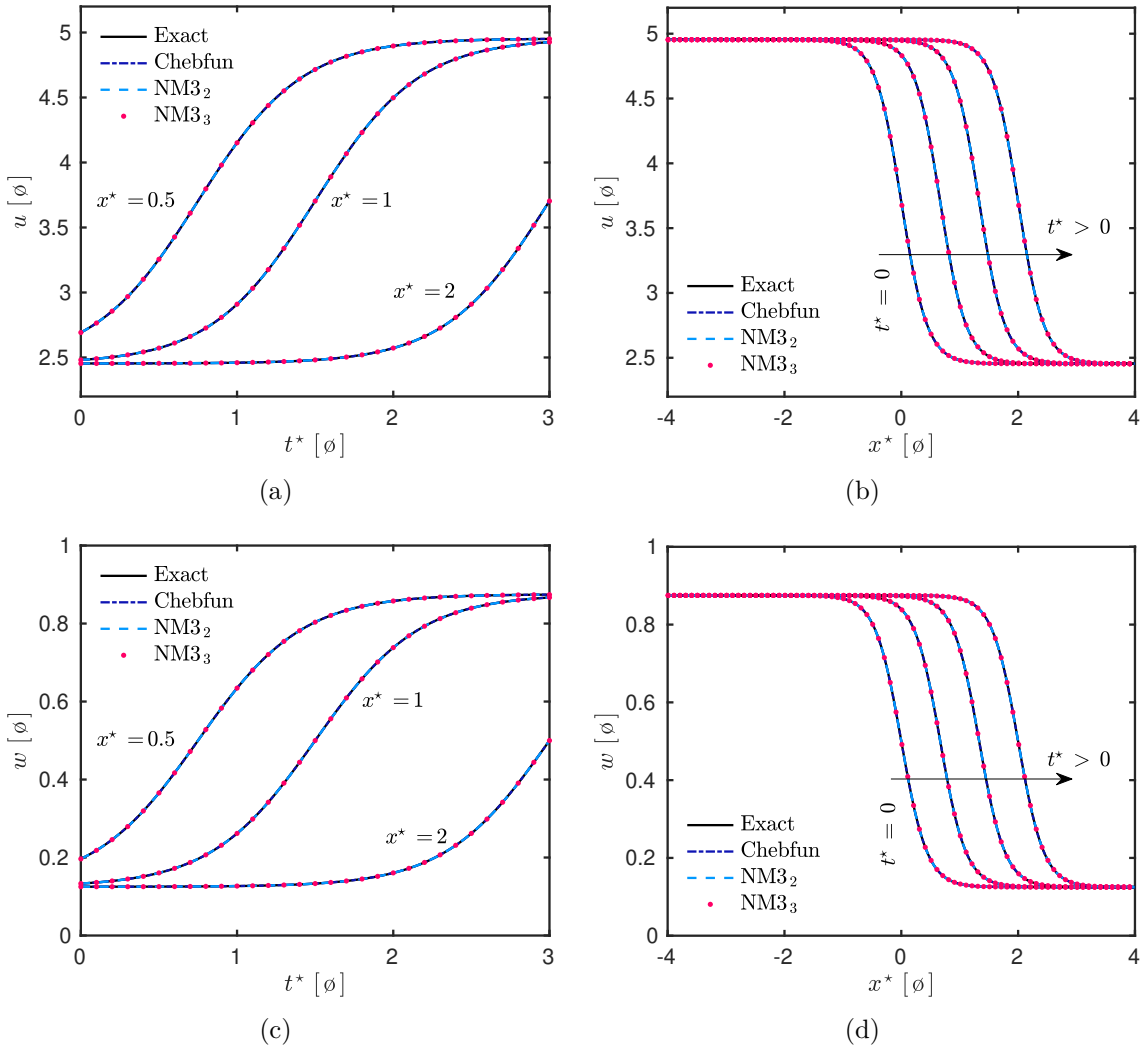

Figure 8. *Time evolution* (a, c) *and profiles* (b, d) *at* $t^\star = \{0, 1, 2, 3\}$ *of the fields* u *and* w *for the second case study.*

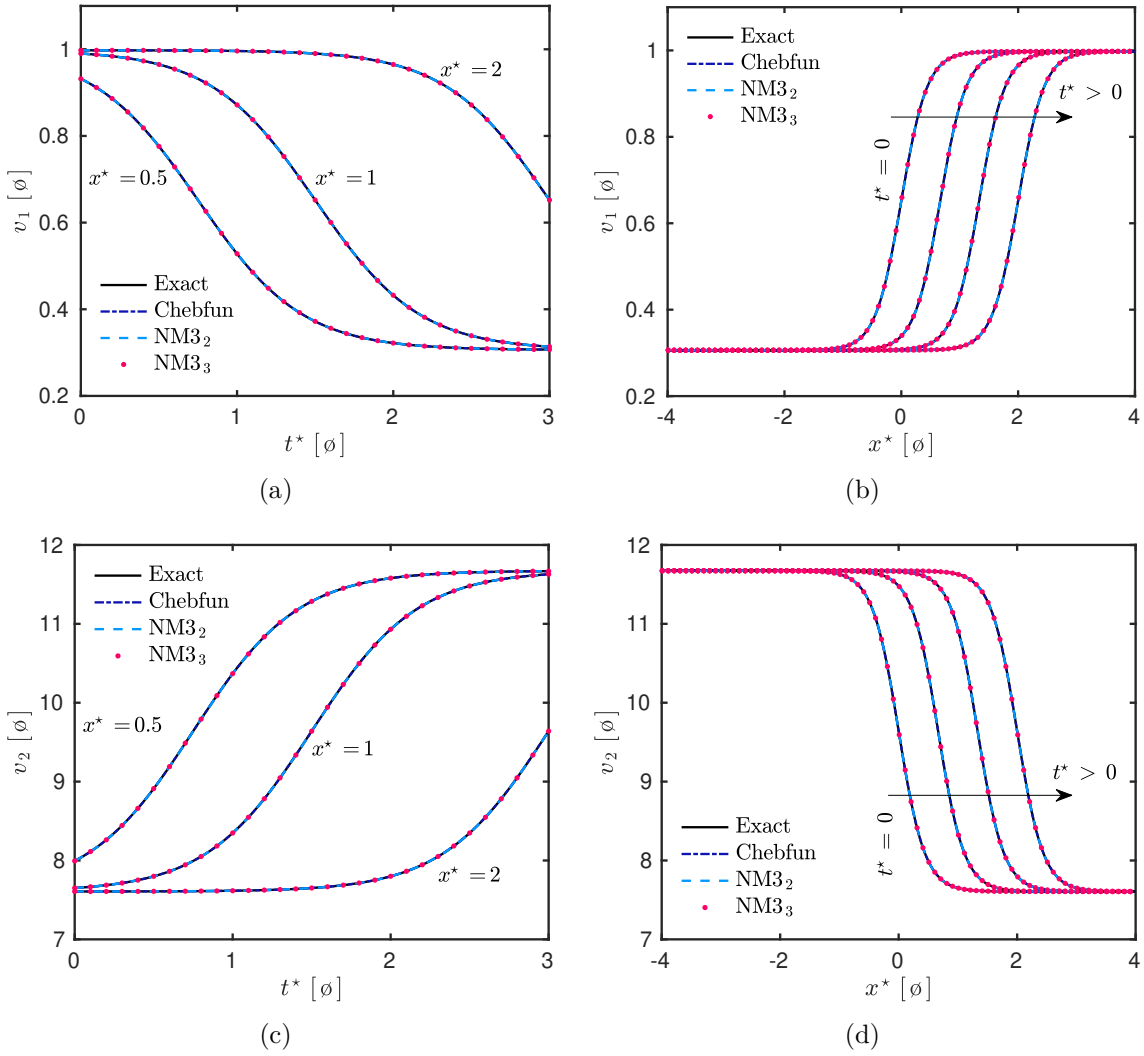

Figure 9. *Time evolution* (a, c) *and profiles* (b, d) *at* $t^\star = \{0, 1, 2, 3\}$ *of the two solutions* v_1 *and* v_2 *for the second case study.*

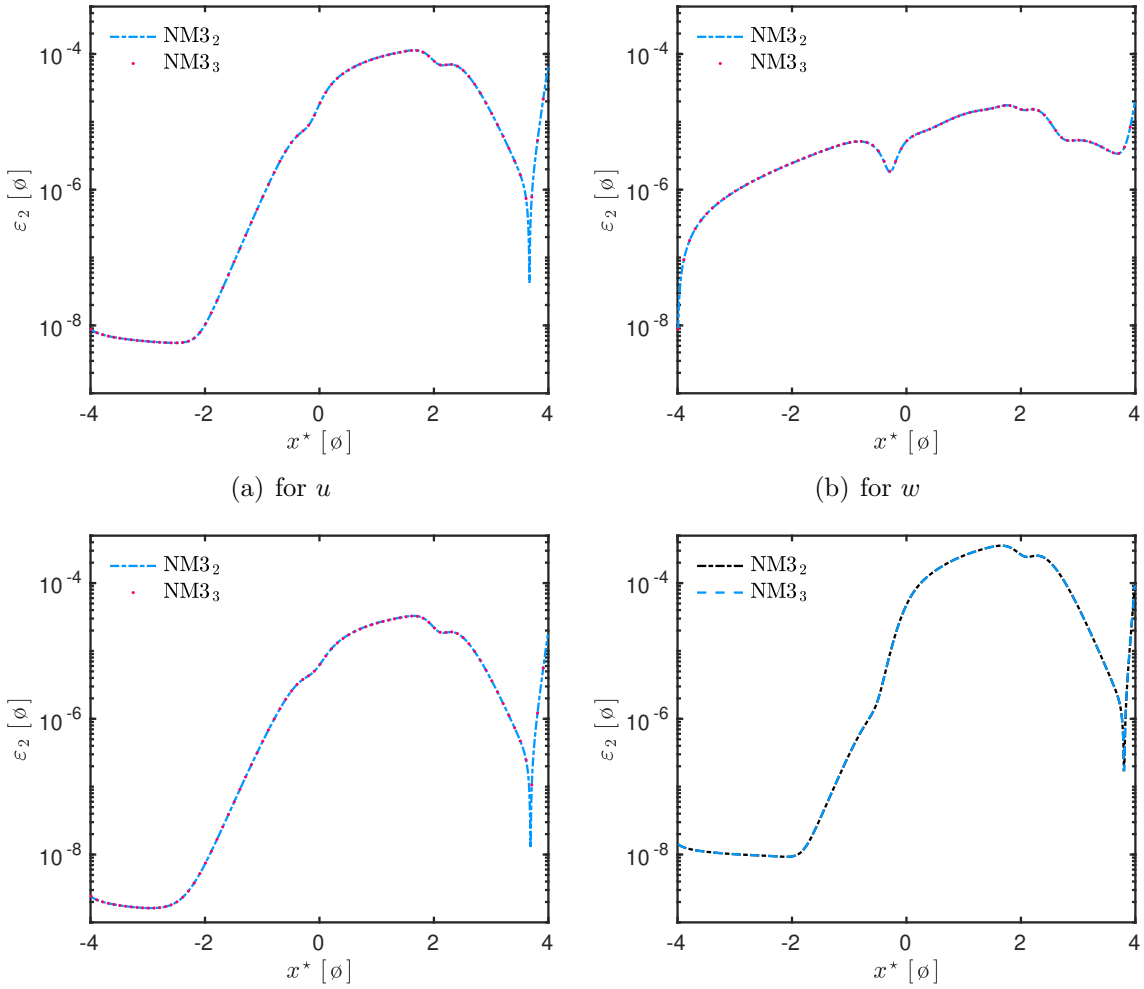

(a) for u (b) for w

(c) for v_1 (d) for v_2

Figure 10. *Variation of the error* ε_2 *of the solutions* u (a), w (b), v_1 (c) *and* v_2 (d) *for the second case study.*

4.3 Third case: Robin boundary conditions and a fully nonlinear problem

The case is illustrated in Figure 2(a). The study is carried out for $x^\star \in \left[\,0\,,\,1\,\right]$ and $t^\star \in \left[\,0\,,\,24\,\right]$. The initial conditions are:

$$u\,(\,x^\star\,,\,0\,)\;=\;v\,(\,x^\star\,,\,0\,)\;=\;w\,(\,x^\star\,,\,0\,)\;=\;\mathbf{0}\,.$$

Robin–type boundary conditions are assumed for the fields u and v:

$$u_{\infty\,,\,L}\;=\;0.8\cdot\sin\!\left(\frac{2\cdot\pi}{10}\cdot t^\star\right)^{6}\,,\quad u_{\infty\,,\,R}\;=\;0.8\cdot\left(\frac{1}{2}\cdot\sin\!\Big(\pi\cdot t^\star\Big)^{\,2}\;+\;\sin\!\left(\frac{2\cdot\pi}{24}\cdot t^\star\right)\right),$$

$$v_{\infty\,,\,L}\;=\;0.9\cdot\sin\!\left(\frac{2\cdot\pi}{3}\cdot t^\star\right)^{2}\,,\quad v_{\infty\,,\,R}\;=\;1.4\cdot\left(\frac{1}{2}\cdot\sin\!\left(\frac{2\cdot\pi}{3}\cdot t^\star\right)^{2}\;+\;\sin\!\left(\frac{2\cdot\pi}{24}\cdot t^\star\right)\right)$$

and the following Biot numbers:

$$\begin{array}{llll}\text{for } x^\star\;=\;0\,, & \mathrm{Bi}_{\,m}\;=\;200\,, & \mathrm{Bi}_{\,q}\;=\;35\,, & \mathrm{Bi}_{\,v}\;=\;10\,,\\ \text{for } x^\star\;=\;1 & \mathrm{Bi}_{\,m}\;=\;125\,, & \mathrm{Bi}_{\,q}\;=\;20\,, & \mathrm{Bi}_{\,v}\;=\;50\,.\end{array}$$

Dirichlet–type boundary conditions are considered for w:

$$w(\,0\,,\,t^\star\,)\;=\;1.3\cdot\left(\sin\!\left(\frac{2\cdot\pi}{6}\cdot t^\star\right)^{2}\;+\;\sin\!\left(\frac{2\cdot\pi}{24}\cdot t^\star\right)\right),$$

$$w(\,1\,,\,t^\star\,)\;=\;0.7\cdot\left(\sin\!\left(\frac{2\cdot\pi}{6}\cdot t^\star\right)^{2}\;+\;1\;+\;\tanh\!\Big(t^\star\;-\;12\Big)\right).$$

The material properties associated to diffusive and advective transfer processes are given by the following dimensionless Fourier and Peclet numbers:

$$\begin{array}{lll}\mathrm{Fo}_{\,m}\;=\;4\cdot10^{-3}\,, & \mathrm{Fo}_{\,q}\;=\;4\cdot10^{-2}\,, & \mathrm{Fo}_{\,a}\;=\;4\cdot10^{-1}\,,\\ \mathrm{Pe}_{\,m}\;=\;2\cdot10^{-3}\,, & \mathrm{Pe}_{\,v}\;=\;3\cdot10^{-3}\,, & \mathrm{Pe}_{\,q}\;=\;5\cdot10^{-3}\,,\end{array}$$

and the following coupling parameters:

$$\gamma\;=\;1.5\cdot10^{-3}\,,\qquad\qquad \delta\;=\;3\cdot10^{-4}\,.$$

The Kossovitch numbers equal to:

$$\begin{array}{lll}\mathrm{Ko}_{\,qv}\;=\;1\cdot10^{-2}\,, & \mathrm{Ko}_{\,qs}\;=\;2\cdot10^{-2}\,, & \mathrm{Ko}_{\,av}\;=\;2\cdot10^{-2}\,,\\ \mathrm{Ko}_{\,as}\;=\;3\cdot10^{-2}\,, & \mathrm{Ko}_{\,at}\;=\;1\cdot10^{-2}\,, & r^\star\;=\;1\,.\end{array}$$

The storage coefficients incorporating the nonlinearity of the material properties are given by:

$$
\begin{aligned}
c_q^\star &= 1 + 0.6 \cdot u^2 + 0.1 \cdot v + 0.3 \cdot w\,, & c_{av}^\star &= 1 + 0.06 \cdot u\,,\\
c_m^\star &= 1 + 0.05 \cdot u^2 + 0.03 \cdot v^2 + 0.01 \cdot w^2\,, & c_{as}^\star &= 1\,,\\
c_a^\star &= 1 + 0.04 \cdot u + 0.03 \cdot v + 0.01 \cdot w\,, & c_{at}^\star &= 1 + 0.03 \cdot v\,,\\
c_{qv}^\star &= 1\,, & c_{qs}^\star &= 1\,.
\end{aligned}
$$

The permeability coefficients are given by:

$$
\begin{aligned}
k_q^\star &= 1 + 0.05 \cdot u + 0.03 \cdot v + 0.01 \cdot w\,,\\
k_v^\star &= 1 + 0.1 \cdot u + 0.01 \cdot u^2 + 0.02 \cdot v + 0.02 \cdot w\,,\\
k_m^\star &= 1 + 0.6 \cdot u + 0.1 \cdot v + 0.3 \cdot w\,,\\
k_a^\star &= 1 + 0.01 \cdot u + 0.02 \cdot u^2 + 0.07 \cdot v^2 + 0.04 \cdot w^2\,.
\end{aligned}
$$

The advection coefficients are:

$$
a_q^\star = \Big(1 + 0.01 \cdot v\Big) \cdot \frac{\partial w}{\partial x^\star}\,, \qquad a_v^\star = \Big(1 + 0.03 \cdot u\Big) \cdot \frac{\partial w}{\partial x^\star}\,.
$$

Finally, the saturation rate σ is defined as:

$$
\sigma \,:\, u \longrightarrow \frac{1}{2} \cdot \Big(1 + \tanh u\Big)\,.
$$

The NM1$_\star$ is employed for the computation of the solution with the discretisation parameters $\Delta x^\star = 0.01$ and $\Delta t^\star = 10^{-4}$, which is consistent with the CFL condition. With higher time discretisation the model does not compute a bounded solution. The numerical models NM3$_2$ and NM3$_3$ are also used with $\Delta t^\star = 2 \cdot 10^{-3}$ and $\Delta x^\star = 10^{-2}$. A pseudo–spectral solution is considered as reference. It is obtained with the `Matlab`™ open source toolbox `Chebfun` [31].

The time evolution of the fields is shown in Figures 11(a), 11(c) and 11(e). For the sake of clarity, only the results computed with NM3 are presented. The fields vary according to the boundary conditions. A good agreement is observed between the solutions and the reference one. Similar conclusions can be drawn for the velocity $\dfrac{\partial w}{\partial x^\star}$ according to Figure 12. The error among the solutions obtained with the numerical models NM3$_2$, NM3$_3$ and NM1$_\star$, and the reference one is shown in Figures 13(a), 13(b) and 13(c). Almost no differences are observed for the fields u and v indicating that the error may arise from the space discretisation and not the temporal scheme. Some differences are noticed in the error of the field w for the numerical model NM3 and NM1$_\star$. They may be due to the temporal scheme and the increase of the discretisation parameter $\Delta t^\star$ between NM1$_\star$ and NM3.

Table 2 reports the computational time required by each model to compute the solution. The numerical model $\mathrm{NM3}_2$ enables to compute the solution ten times faster than $\mathrm{NM1}_\star$ for the same order of accuracy ε_∞. This ratio becomes six times for the numerical model $\mathrm{NM3}_3$. Since the number of operations to do between two–step Runge–Kutta approaches for $s = 2$ and for $s = 3$ is multiplied by two (with same discretisation parameters), these results are consistent. One important result is the relaxation of the stability condition. The two–step Runge–Kutta scheme enables to reduce the restriction by twenty times.

This case highlights the efficiency of the proposed numerical models for real applications with a very satisfactory accuracy and a reduced computational time compared to more conventional approaches.

Table 2. *Computational time required by the numerical models to compute the solution of the third case study (Section 4.3), with* $t_{\max} = 84 \left[\mathsf{s}\right]$ *and* $\Delta t_{\min} = 10^{-4}$.

Numerical Model (NM)	$\Delta x^\star$	$\Delta t^\star$	ε_∞	CPU time
$\mathrm{NM1}_\star$	10^{-2}	$\Delta t_{\min}$	$6.1 \cdot 10^{-3}$	$t_{\max}$
$\mathrm{NM3}_2$	10^{-2}	$20 \cdot \Delta t_{\min}$	$7.4 \cdot 10^{-3}$	$0.09 \cdot t_{\max}$
$\mathrm{NM3}_3$	10^{-2}	$20 \cdot \Delta t_{\min}$	$7.4 \cdot 10^{-3}$	$0.15 \cdot t_{\max}$

5 Conclusion

In the context of predicting the physical phenomena of heat, air and moisture transfer in porous material, it is of major importance to build efficient numerical models that maximize the accuracy and minimize the computational efforts. However, the task is ambitious considering the numerical issues of the mathematical model to predict highly coupled advective–diffusive phenomena. The model is composed of a system of two advection–diffusion differential equations plus one purely diffusion equation. Two major numerical issues are identified to propose an efficient numerical model. First, a very restrictive stability condition is imposed if one uses classical explicit Euler approaches. Second, the high nonlinearities in the problem may become prohibitive to the use of implicit methods. Indeed, even if the stability restrictions are overcome, they impose costly subiterations that do not save computational efforts.

Hence, this paper proposes an efficient numerical model to solve these difficulties. As described in Section 3, it is based on a promising combination of three innovative numerical approaches. The first one is the so-called Du Fort–Frankel approach that builds an explicit scheme with extended stability restrictions for the computation of purely diffusion equation. The two advection–diffusion equations are solved using the Scharfetter–Gummel scheme for the space discretisation combined with an explicit two-step Runge–Kutta method. This combination enables to relax the standard stability restriction up to

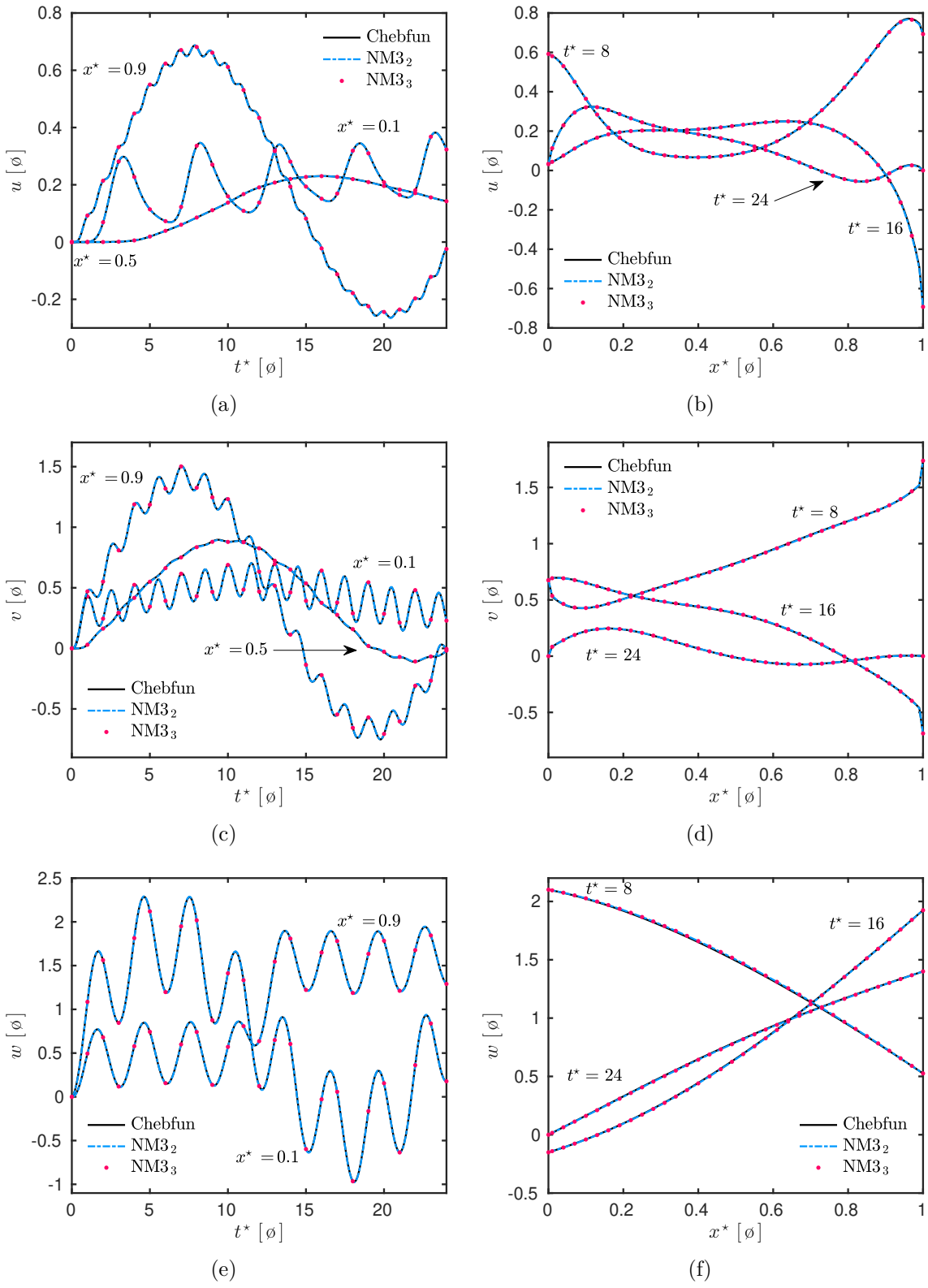

Figure 11. (a, c, e) *Time evolution and* (b, d, f) *profiles of the fields* u , v *and* w *for the third case study.*

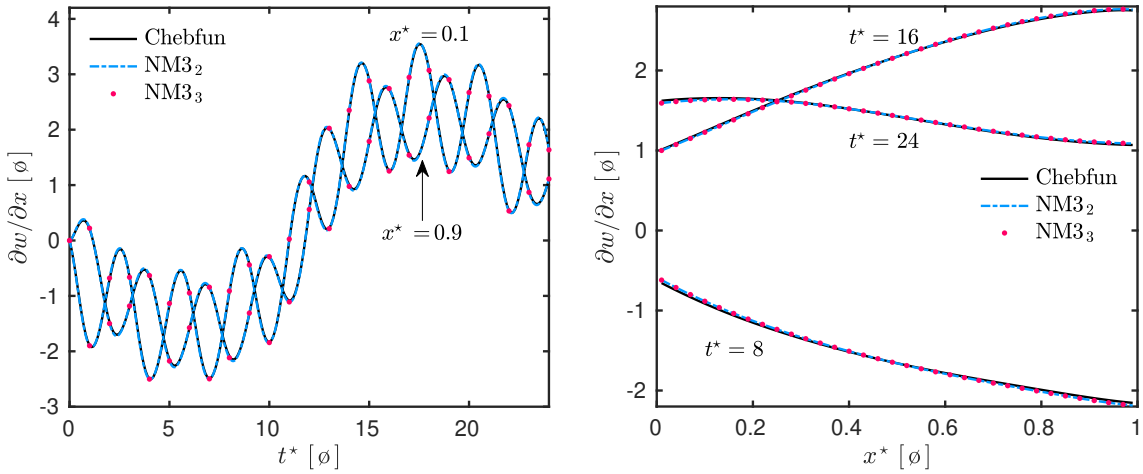

(a) for u (b) for v_1

Figure 12. (a) *Time evolution and* (b) *profiles of the velocity* $\dfrac{\partial w}{\partial x^\star}$ *for the third case study.*

$\Delta t \leqslant \mathcal{O}\big(5\big)\cdot\Delta x$ for these two equations. At the end, an explicit scheme with a strongly relaxed stability conditions is obtained. Furthermore, the SCHARFETTER–GUMMEL scheme is well balanced and asymptotically preserving to handle strong variations of advection and diffusion coefficients [22].

To validate the numerical efficiency of the proposed numerical model, three validation cases have been considered. The first one assumed quasi-linear coefficients allowing the verification of the theoretical results. Indeed, the stability condition is relaxed by a factor of 40 compared to a standard approach based on explicit EULER time discretisation. The second case proposed an analytical solution for a slightly nonlinear case. To our knowledge, this solution has never been proposed in the literature and may be useful for the validation of numerical models from other researchers. A very satisfying accuracy at the order $\mathcal{O}(10^{-4})$ is observed for the proposed model using discretisation parameters $\Delta x^\star = 10^{-2}$ and $\Delta t^\star = 10^{-4}$. The last case study dealt with a more realistic application where coefficients are nonlinear. ROBIN-type boundary conditions varying in time are assumed. A very good agreement has been observed with the reference solution obtained with the `Matlab`™ open source toolbox `Chebfun` [31]. Moreover, the computational time is divided by 10 compared to the standard approaches for the same level of accuracy. These three case studies enhance the possibility to build an efficient numerical model for real applications with minimized computational efforts and a very satisfactory accuracy. It is important to remark that if the numerical stability restrictions is relaxed thanks to the innovative schemes, the choice of the time discretisation has to be made according to the characteristic time of the physical phenomena. Further research should focus on the extension of the numerical model to multi-dimensional transfer.

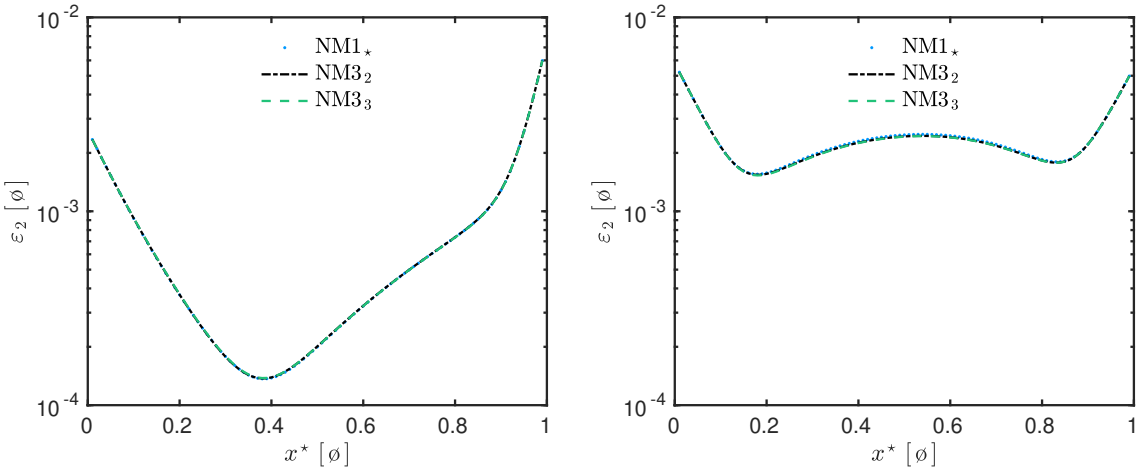

(a) for u (b) for v_1

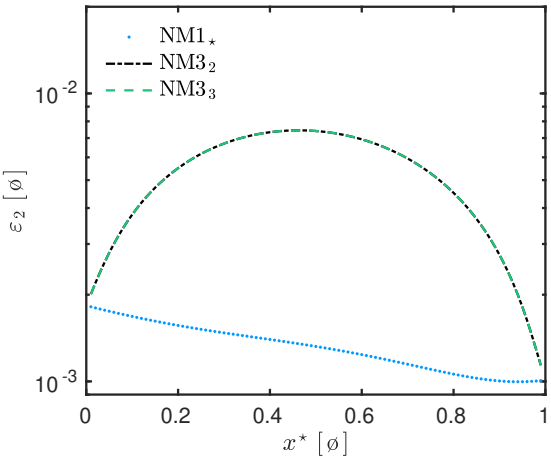

(c) for w

Figure 13. *Variation of the error ε_2 of the solutions u* (a), *v* (b) *and w* (c) *for the third case study.*

6 Nomenclature

Latin letters		
a_q	heat advection coefficient	$[\mathsf{W/(m^2 \cdot K)}]$
a_v	vapor advection coefficient	$[\mathsf{s/m}]$
c	specific heat	$[\mathsf{J/(kg \cdot K)}]$
c_{at}	storage coefficient	$[\mathsf{kg \cdot Pa/(J \cdot K)}]$
c_m	moisture storage capacity	$[\mathsf{kg/(m^3 \cdot Pa)}]$
c_q	volumetric heat capacity	$[\mathsf{J/(m^3 \cdot K)}]$
c_{qs} , c_{as}	storage coefficient	$[\mathsf{kg \cdot Pa/J}]$
c_{qv} , c_a , c_{av}	storage coefficient	$[\mathsf{kg/J}]$
k_a	permeability coefficient	$[\mathsf{s^2/m^2}]$
k_q	thermal conductivity	$[\mathsf{W/(m \cdot K)}]$
L	length	$[\mathsf{m}]$
m	mass	$[\mathsf{kg}]$
P , P_1	pressure	$[\mathsf{Pa}]$
r_{12}	latent heat of evaporation	$[\mathsf{J/kg}]$
T	temperature	$[\mathsf{K}]$
t	time coordinate	$[\mathsf{s}]$
x	space coordinate	$[\mathsf{m}]$

Greek letters		
α_m	surface vapour transfer coefficient	$[\mathsf{s/m}]$
α_q	surface heat transfer coefficient	$[\mathsf{W/(m^2 \cdot K)}]$
σ	saturation rate	$[\varnothing]$

Acknowledgments

The authors acknowledge the Junior Chair Research program “Building performance assessment, evaluation and enhancement” from the University of Savoie Mont Blanc in collaboration with The French Atomic and Alternative Energy Center (CEA) and Scientific and Technical Center for Buildings (CSTB). The authors also acknowledge the French and Brazilian agencies for their financial supports through the project CAPES–COFECUB, as well as the CNPQ of the Brazilian Ministry of Education and of the Ministry of Science, Technology and Innovation, respectively, for co-funding.

References

[1] T. Defraeye. Advanced computational modelling for drying processes – a review. *Applied Energy*, 131:323–344, 2014. 2

[2] N. Mendes, M. Chhay, J. Berger, and D. Dutykh. *Numerical methods for diffusion phenomena in building physics*. PUCPress, Curitiba, Brazil, 2016. 2

[3] H. Davarzani, K. Smits, R.M. Tolene, and T. Illangasekare. Study of the effect of wind speed on evaporation from soil through integrated modeling of the atmospheric boundary layer and shallow subsurface. *Water resources research*, 50(1):661–680, 2014. 2

[4] S. Rouchier, T. Busser, M. Pailha, A. Piot, and M. Woloszyn. Hygric characterization of wood fiber insulation under uncertainty with dynamic measurements and Markov Chain Monte-Carlo algorithm. *Building and Environment*, 114:129–139, mar 2017. 2

[5] T. Colinart, D. Lelievre, and P. Glouannec. Experimental and numerical analysis of the transient hygrothermal behavior of multilayered hemp concrete wall. *Energy and Buildings*, 112:1 – 11, 2016. 2

[6] C. Belleudy, M. Woloszyn, M. Chhay, and M. Cosnier. A 2d model for coupled heat, air, and moisture transfer through porous media in contact with air channels. *International Journal of Heat and Mass Transfer*, 95:453 – 465, 2016. 2, 3

[7] B. Remki, K. Abahri, M. Tahlaiti, and R. Belarbi. Hygrothermal transfer in wood drying under the atmospheric pressure gradient. *International Journal of Thermal Sciences*, 57:135 – 141, 2012. 2

[8] K. Abahri, R. Bennacer, and R. Belarbi. Sensitivity analyses of convective and diffusive driving potentials on combined heat air and mass transfer in hygroscopic materials. *Numerical Heat Transfer, Part A: Applications*, 69(10):1079–1091, 2016. 2, 3

[9] J. Berger, D. Dutykh, N. Mendes, and B. Rysbaiuly. A new model for simulating heat, air and moisture transport in porous building materials. *International Journal of Heat and mass Transfer*, 134(-):1041–1060, 2019. 2, 3, 4

[10] A.V. Luikov. *Heat and Mass Transfer in Capillary-Porous Bodies*. Pergamon, Oxford, 1966. 3

[11] G.H. Dos Santos and N. Mendes. Heat, air and moisture transfer through hollow porous blocks. *International Journal of Heat and Mass Transfer*, 52(9):2390 – 2398, 2009. 3

[12] R. Courant, K. Friedrichs, and H. Lewy. Über die partiellen Differenzengleichungen der mathematischen Physik. *Mathematische Annalen*, 100(1):32–74, 1928. 3, 7

[13] C. Zoppou. *Numerical solution of the advective-diffusion equation*. Australian National University, 1994. 3

[14] D. J. Duffy. A critique of the Crank–Nicolson scheme strengths and weaknesses for financial instrument pricing. *Wilmott*, BV 2004(4):68–76, 2004. 3

[15] W. Kahan and J. Palmer. On a proposed floating-point standard. *ACM SIGNUM Newsletter*, 14(-):13–21, 1979. 4

[16] A. Nayfeh. *Perturbation Methods*. Wiley VCH, New York, 2000. 4

[17] J. Berger, S. Gasparin, D. Dutykh, and N. Mendes. Accurate numerical simulation of moisture front in porous material. *Building and Environment*, 118(-):211 – 224, 2017. 7

[18] J. Berger, S. Gasparin, D. Dutykh, and N. Mendes. On the solution of coupled heat and moisture transport in porous material. *Transport in Porous Media*, (-):1–38, 2017. 7, 12, 16

[19] J. Chollom and Z. Jackiewicz. Construction of two-step Runge–Kutta methods with large regions of absolute stability. *Journal of Computational and Applied Mathematics*, 157(1):125 – 137, 2003. 7, 13, 14

[20] D. L. Scharfetter and H. K. Gummel. Large-signal analysis of a silicon read diode oscillator. *IEEE Transactions on Electron Devices*, 16(1):64–77, 1969. 9

[21] L. Gosse. *Computing Qualitatively Correct Approximations of Balance Laws*. Springer-Verlag, Italia, 2013. 9

[22] L. Gosse and R. Natalini. *Chapter 6: Viscous equations treated with L-splines and Steklov-Poincaré operator in two dimensions*, volume 16. Springer International Publishing, 2017. 9, 16, 36

[23] L. Gosse. L-splines and viscosity limits for well-balanced schemes acting on linear parabolic equations. *Acta Applicandae Mathematicae*, 153(1):101–124, 2018. 9, 16

[24] Z. Jackiewicz, R. Renaut, and A. Feldstein. Two-Step Runge–Kutta Methods. *SIAM Journal on Numerical Analysis*, 28(4):1165–1182, 1991. 13

[25] H. Kreiss and G. Scherer. Method of lines for hyperbolic differential equations. *SIAM Journal on Numerical Analysis*, 29(3):640–646, 1992. 14

[26] E. C. Du Fort and S. P. Frankel. Stability conditions in the numerical treatment of parabolic differential equations. *Mathematical Tables and Other Aids to Computation*, 7(43):135–152, 1953. 14

[27] S. Gasparin, J. Berger, D. Dutykh, and N. Mendes. Stable explicit schemes for simulation of nonlinear moisture transfer in porous materials. *Journal of Building Performance Simulation*, (-), 2017. 15

[28] P. J. Taylor. The stability of the Dufort-Frankel method for the diffusion equation with boundary conditions involving space derivatives. *The Computer Journal*, 13(1):92, 1970. 15

[29] S. Gasparin, J. Berger, D. Dutykh, and N. Mendes. An improved explicit scheme for whole-building hygrothermal simulation. *Building Simulation*, (-), 2017. 15

[30] G. Söderlind and L. Wang. Evaluating numerical ODE/DAE methods, algorithms and software. *Journal of Computational and Applied Mathematics*, 185(-):244–260, 2006. 17

[31] T. A. Driscoll, N. Hale, and L. N. Trefethen. Chebfun guide. *Pafnuty Publications*, (-), Oxford 2014. 19, 28, 33, 36

[32] A. Tychonoff. Théorèmes d'unicité pour l'équation de la chaleur (in French). *Mat. Sb.*, 31(2):199–216, 1935. 28